Ground-ice origin and age on Herschel Island (Qikiqtaruk), Yukon, Canada

Sebastian Wetterich [a],[*],[1], Alexander I. Kizyakov [b], Thomas Opel [c], Hendrik Grotheer [d],
Gesine Mollenhauer [d], Michael Fritz [a]

[a] *Alfred Wegener Institute Helmholtz Centre for Polar and Marine Research, Permafrost Research Section, 14473, Potsdam, Germany*
[b] *Lomonosov Moscow State University, Faculty of Geography, Department of Cryolithology and Glaciology, 119991, Moscow, Russia*
[c] *Alfred Wegener Institute Helmholtz Centre for Polar and Marine Research, Polar Terrestrial Environmental Systems Section, 14473, Potsdam, Germany*
[d] *Alfred Wegener Institute Helmholtz Center for Polar and Marine Research, Marine Geochemistry Section, 27570, Bremerhaven, Germany*

ARTICLE INFO

ABSTRACT

Glacial legacies preserved in permafrost such as buried glacial ice of the last ice age are of increasing concern in the Western Canadian Arctic. Permafrost collapse due to melting ground ice largely follows the margins of the maximum Laurentide Ice Sheet extent and therefore predetermines the postglacial landscape evolution in this region. Another type of ground ice, (i.e., wedge ice) of late Pleistocene and Holocene age associated with permafrost aggradation, is also widespread here. Our study on Herschel Island (Qikiqtaruk, Beaufort Sea) re-examines previous data and applies stable-isotope and dissolved organic carbon (DOC) analyses as well as radiocarbon dating on DOC and particulate plant macrofossil remains preserved in massive ground ice, wedge ice and host deposits.

Newly obtained DOC ages of the massive ice span from 32 220 to 25 830 cal BP and extend the only previously available direct age determination (CO_2-derived radiocarbon age of 21 290 cal BP) properly into the Last Glacial Maximum as the formation time of the massive ice. Its newly obtained isotopic composition exhibits mean values of -33.1 ± 0.6‰ in δ^{18}O, of -257 ± 4‰ in δD and 7.6 ± 0.9‰ in deuterium excess (*d*) fitting into previously reported respective data ranges. The very low (negative) stable isotope composition of the massive ice, the numerous enclosed spherical air bubbles as well as the very low mean DOC content of 0.7 ± 0.1 mg L^{-1} provide strong evidence for an origin as glacier ice that was buried and has survived since deglaciation.

The newly studied wedge ice on Herschel Island formed during the Holocene between 9220 and 3470 cal BP, and shows a distinct isotopic composition with mean values of -18.4 ± 1.1‰ in δ^{18}O, -138 ± 9‰ in δD and a mean deuterium excess (*d*) of 8.8 ± 1.4‰. Such isotopic wedge-ice record as well as its mean DOC concentration of 4.3 ± 2.1 mg L^{-1} fall within the range of previously studied Holocene ice wedges in the region. The directly-dated stable isotope record of ice-wedge growth on Herschel Island indicates a winter cooling trend towards the mid-Holocene, even though most available records attribute this cooling rather to the warm season while the winter temperatures over this period are not constrained yet.

The extraordinarily rich ground-ice inventory of Herschel Island offers insights into the glacial and postglacial landscape evolution of the Western Canadian Arctic. Here, paleoenvironmental research highlights ice sheet-permafrost interactions over glacial, deglacial and postglacial timescales.

1. Introduction

Ground ice constitutes a substantial component in sedimentary permafrost deposits (e.g., French and Shur, 2010). Permafrost aggradation leads to sub-surface freezing of sediments with the formation of pore ice (by *in-situ* moisture freezing in capillary spaces) and segregated ice (by water migration to the freezing front) forming ice lenses on micro-to macroscale (mm to cm). Thermal ground-contraction in a polygonal pattern promotes frost cracking during the cold season followed by warm-season crack filling mainly by snowmelt and snow

---

producing vertical ice veins that might grow into ice wedges if the mechanism is repeated over decades to millennia (Lachenbruch, 1962).

Another type of permafrost ground ice is massive (or tabular) ice that is widespread both in the Eurasian and North American Arctic. A database and map of massive ice in the Arctic were compiled by Streletskaya et al. (2002) after collecting and analyzing observation data on the distribution and properties of massive ground ice. Streletskaya et al. (2002) note that massive ground ice is not observed in northeastern Siberia where a long-term continental sedimentation regime took place during the late Pleistocene. Meanwhile, tabular massive ice is most widespread in areas of Pleistocene marine transgressions, in particular in northwestern Siberia. Here, the massive ground ice is considered as intra-sedimental segregation ice reaching thicknesses of tens of meters (Parmuzin and Sukhodol'skiy, 1982; Dubikov, 2002; Streletskaya et al., 2013). However, its formation might also be associated with more or less extensive glaciations (Ingólfsson and Lokrantz, 2003). If present, such

glacial legacies are preserved within permafrost as buried glacier ice or basal regelation ice (Kokelj et al., 2017). The origin of massive ice bodies as buried glacial ice, segregated or segregated-intrusive ice is still debated along the marginal regions of late-Pleistocene glaciations (Dalton et al., 2022), not only in the realm of the Kara-Scandinavian Ice Sheet in West Siberia (Ingólfsson and Lokrantz, 2003) but also for the Laurentide-Innuitian Ice Sheet in northwestern Canada (Coulombe et al., 2019; Lacelle et al., 2018; Murton et al., 2005).

The occurrence of near-surface massive ice promotes a high vulnerability of permafrost to thaw under mechanical and/or thermal disturbance. Rising summer air temperatures and active layer deepening lead to permafrost degradation, including the formation of retrogressive thaw slumps (RTS) at river and lake shores (Kokelj et al., 2017; Lantuit and Pollard, 2008; Lantz et al., 2008) as well as at Arctic sea coasts and inland locations (Lakeman and England, 2012; Lewkowicz and Way, 2019; Segal et al., 2016). Where massive ice becomes exposed, the
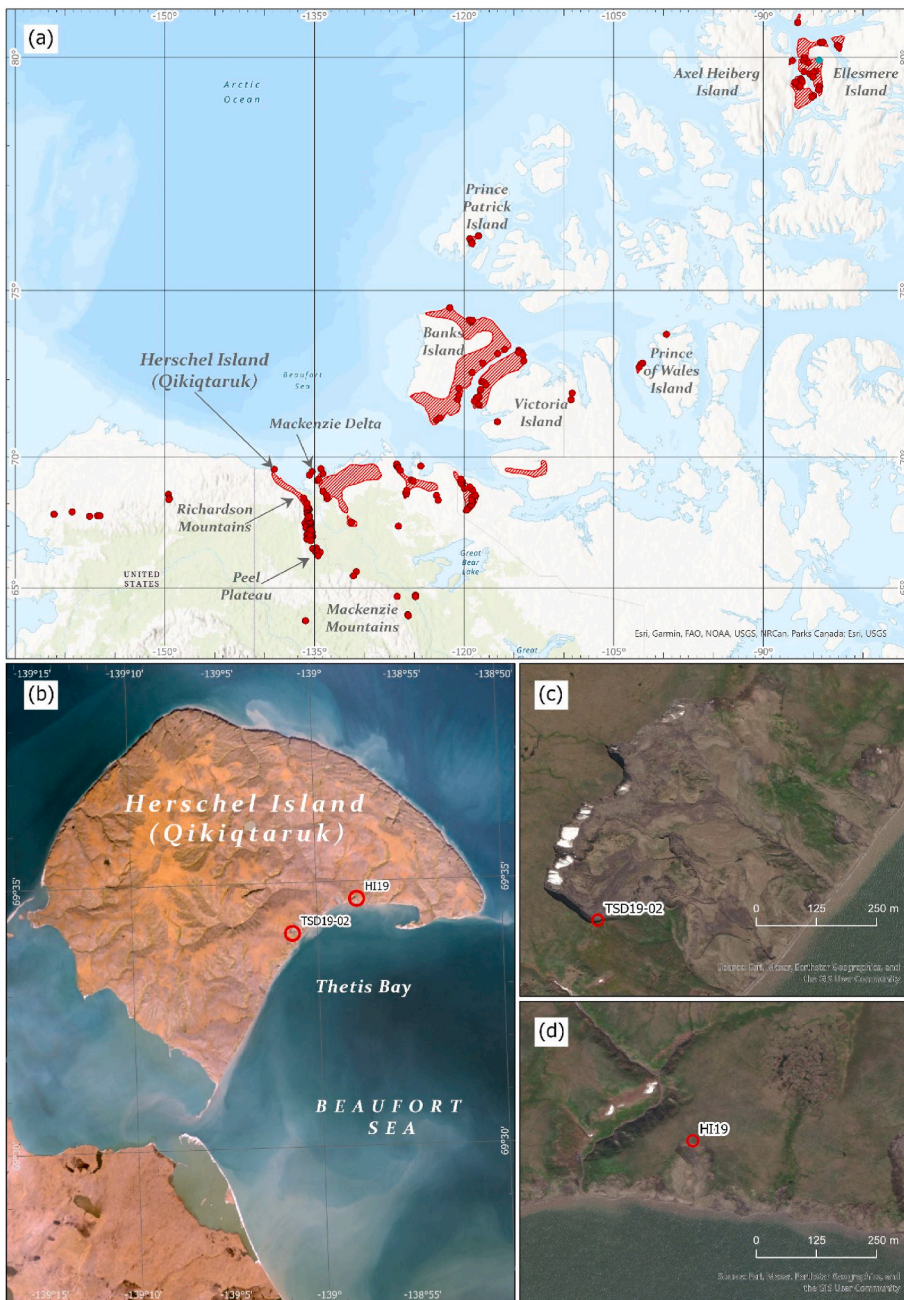
Fig. 1. Location maps showing (a) the distribution of reported locations of large retrogressive thaw slumps in Canada (based on Kokelj and Lewkowicz, 1999; Kokelj et al., 2009, 2017; Lacelle et al., 2004, 2015; Lewkowicz and Way, 2019; Ramage et al., 2017; Wang et al., 2016; Ward Jones et al., 2019), (b) a satellite image of Herschel Island (Sentinel-2 imagery, 07 September 2021) with sampling locations detailed (c) for the massive-ice profile TSD19-02 and (d) for the wedge-ice profile HI19. Red shaded areas in panel (a) indicate widespread occurrences of RTSs. Panel (a) is based on the ESRI Basemap World Topographic Map. Panels (c) and (d) are based on ESRI Basemap World Imagery. (For interpretation of the references to colour in this figure legend, the reader is referred to the Web version of this article.)

formation of RTS is controlled by processes of thermal denudation such as active-layer detachments, ice melt, thaw of the frozen host deposits, headwall and thermo-terrace formation as well as slumping and transport of thawed material in mudflows. On Arctic sea coasts with exposed ice-rich permafrost, thermal denudation and thermal abrasion interact (Günther et al., 2013). For RTS, high headwall retreat rates are common, which might reach up to a few tens of meters per year (Lantz et al., 2008; Lantuit and Pollard, 2008). RTS are confined to the areas of distribution of both massive ground ice and other ice-rich deposits reaching for example up to 87% volumetric ice content in Ice Complex permafrost deposits of the Batagay megaslump in northeastern Siberia (Kizyakov et al., 2023). In these regions actively growing RTS are widely represented. Other well-known RTS sites in Eurasia are found on Kolguev Island (Kizyakov et al., 2013), in northwestern Siberia on the peninsulas Yugorsky (Kizyakov et al., 2006; Leibman et al., 2021) and Yamal (Khomutov et al., 2017; Nesterova et al., 2021), in the central regions of Yakutia (Kunitsky et al., 2013; Murton et al., 2022), and in northeastern Siberia in the coastal regions and on the Arctic islands of Yakutia (Pizhankova and Dobrynina, 2010; Günther et al., 2013, 2015) and Chukotka (Maslakov et al., 2021; Runge et al., 2022). North American RTS sites (Fig. 1a) are reported from the Western Canadian Arctic on Herschel Island (Lantuit et al., 2012), from the northern parts of continental Alaska and Canada (Lacelle et al., 2004, 2015; Kokelj et al., 2017; Lantz et al., 2008), and in the Canadian Arctic Archipelago (Lewkowicz and Way, 2019; Ward Jones et al., 2019).

The actively retreating headwalls of RTS reveal unique natural outcrops for detailed structural, geochemical, sedimentological and paleontological studies of ground ice and its host deposits in order to address paleoclimatic, paleogeographical and paleoenvironmental research questions of the respective region (Ashastina et al., 2018; Opel et al., 2019). Commonly applied methods of cryostratigraphy, ice crystallography, hydrochemistry and stable water-isotope geochemistry on massive ice bodies aim to deduce the formation and preservation conditions of the ice as well as the glaciation extents in space and time (Lorrain and Demeur, 1985). The stable isotope composition of oxygen ($\delta^{18}O$) and hydrogen (δD) of ground ice preserves information on its origin and formation conditions (Lacelle and Vasil'chuk, 2013; Opel et al., 2018), and is therefore widely applied in paleoclimatic and permafrost research (Porter and Opel, 2020).

Reliable chronologies are mandatory to resolve timing, origin and formation of ground ice and often employ either radiocarbon-dated organic material of the host deposits or direct dating of organic material from inside the ice bodies. The latter might be applied for macroscopic floral and faunal fossils found within the ice to constrain up to centennial resolution of composite ice-wedge chronologies of multi-sites (Meyer et al., 2010, 2015) or single-sites (Opel et al., 2017; Wetterich et al., 2020, 2021). Alternatively, dissolved organic carbon (DOC) also serves as source of age information from wedge ice and is increasingly used (Lachniet et al., 2012) as it preserves the timing of ground-ice formation by dating snowmelt-leached DOC that enters the frost crack of forming wedge ice (Fritz et al., 2015). Ice-wedge chronologies based on DOC dating demonstrated that such approach potentially avoids overestimates which might occur due to the incorporation of re-located particulate organic (old) material predating the ice wedge (Campbell-Heaton et al., 2021a, 2021b; Grinter et al., 2019; Holland et al., 2020). DOC concentrations vary strongly for different ground ice types along the Yukon coast. Tanski et al. (2016) reported a median DOC concentration of 8.0 mg L^{-1} in ice wedges and of 1.1 mg L^{-1} in massive ice beds. This is in good agreement with a pan-Arctic study by Fritz et al. (2015), with a mean DOC concentration of 9.6 mg L^{-1} for ice wedges and 1.7 mg L^{-1} for presumably basal glacier ice from the Yukon Coast including Herschel Island.

Herschel Island (Qikiqtaruk, Yukon Coastal Plain, Beaufort Sea; Fig. 1a) formed as a push moraine presumably of the last glacial advance during the Late Wisconsin although direct age information is scarce (Fritz et al., 2011, 2012; Mackay, 1959; Moorman et al., 1996) and

earlier formation of the moraine during the Early Wisconsin has been proposed (Rampton, 1982). The cryolithological inventory comprises massive ice that builds-up substantial parts of the island and that is widely exposed at RTSs at Thetis Bay (Fig. 1b; up to 15 m exposed thickness) and the northwestern coast (Burn, 2012). The massive ice underlies icy silts and clays of marine origin, while terrestrial permafrost including ice wedges and intra-sedimental ice characterizes the uppermost horizons (up to several meters thick) and is in places expressed as polygon tundra in the surface relief (Fritz et al., 2016; Pollard, 1990). The ice-wedge cryostratigraphy on Herschel Island differentiates into generations of Late Wisconsin truncated epigenetic ice wedges (below a thaw unconformity) dated to ca. 16-11 cal ka BP, and of middle to late Holocene syngenetic ice wedges (above a thaw unconformity) dated to ca. 6.5 cal ka BP to present yet (Fritz et al., 2012). However, direct age information from ground-ice records to shed light on landscape evolution on Herschel Island is still scarce, especially the formation of the massive ice as buried glacial ice or basal regelation ice as legacy of the furthest glacial advance at the northwestern margin of the Laurentide Ice Sheet (LIS) still needs refinement (Fritz et al., 2011; Moorman et al., 1996).

In this context, the present study aims (1) to provide newly obtained stable oxygen and hydrogen isotope data of both prevailing ground-ice types on Herschel Island – massive ice and wedge ice – to complement pre-existing datasets, (2) to apply for the first time direct radiocarbon dating of DOC from both ground-ice types in comparison to plant macrofossil dating to obtain insights into the formation timing of distinct cryostratigraphic horizons, and (3) to discuss the new ground-ice records from Herschel Island in the broader context of glacial and postglacial landscape evolution in the Western Canadian Arctic.

2. Study site

The climate of the northern Yukon is characterized by distinct seasonality with long harsh winters and short warm summers at a mean annual air temperature of −11 °C, and a low mean annual precipitation of 161 mm (at Komakuk Beach mainland coast ca. 40 km west of Herschel Island; 1971–2000; Burn and Zhang, 2009).

Herschel Island belongs to the region of continuous permafrost distribution (Obu et al., 2019). At Collinson Head on the island, the annual zero-amplitude depth at a mean annual ground temperature of −8 °C was found at 14.5 m and the seasonally thawed uppermost (active layer) reached depths between 0.4 and 0.7 m (2003–2007; Burn and Zhang, 2009).

The island measures about 15 by 8 km across and rises up to about 180 m above sea level (asl). The ground is built of unconsolidated redeposited marine and terrestrial frozen deposits mixed into a glacial diamicton (glaciotectonite; Rampton, 1982). A generally high surface dissection is seen in intensive gullying through thermal erosion and locally variable ground subsidence and thermokarst through thawing permafrost (Lenz et al., 2013; Fritz et al., 2018). These processes provide Herschel Island with a high spatial and temporal variability in surface relief and disturbance regime (Obu et al., 2017). The ground ice volumes on Herschel Island exceed 50% (Couture, 2010) seen in the high vulnerability of permafrost to thaw and leading to accelerated active-layer detachments, retrogressive thaw slumping and coastal erosion (Obu et al., 2016).

The vegetation on Herschel Island is classified as erect dwarf shrub tundra in the Circumpolar Arctic Vegetation Map (Walker et al., 2005) with sedges (*Carex* sp.) dominating sites with impeded drainage, and tussock cottongrass (*Eriophorum vaginatum*) dominating better drained, elevated surfaces (Wolter et al., 2016).

3. Material and methods

3.1. Fieldwork and on-site observations

The sampling of ground ice on Herschel Island was conducted in early August 2019. Two locations with accessible and safe exposures at the shore of the Thetis Bay (Fig. 1) were chosen to sample massive ice (profile ID: TSD19-02; 69.56752 °N, 139.02258 °W) and wedge ice (profile ID: HI19; 69.57787 °N, 138.96385 °W).

The TSD19-02 profile was sampled at the western edge of Herschel island's largest thaw slump (named as thaw slump D; Lantuit and Pollard, 2008) at the headwall above the slump floor (Figs. 1c and 2a, b). The overlying deposits differentiated into a colluvium cover (as described for profile HI19 below) reaching 2.2 m below surface (bs), including the uppermost active layer of 1 m thickness. Between 2.2 and 6 m b grey clayish diamicton is exposed including pebbles and cobbles as previously described by Fritz et al. (2011). The deposit is very ice-rich with horizontal cryostructures formed by 30–60 mm thick ice layers. The intra-sedimental ice includes air bubbles 2–3 mm in diameter arranged in a chain-like pattern. The distance between the ice layers decreases from 5 to 10 cm in the upper part (ca. 2.2–3 m bs) to 2–5 cm in the middle part (ca. 3–4 m bs) of the diamicton unit, indicating the increasing ice content with depth toward the underlying massive ice. Below 4.2 m bs the cryostructure changes to irregularly distributed large horizontal and sub-horizontal ice layers, 50–70 mm thick and 10–50 cm long. The cryostructure between the horizontal ice layers is irregularly reticulated or lenticular. Organic inclusions of the diamicton comprise broken marine mollusc shells (found at 4.3 m bs) and plant remains (twigs found *in-situ* at 4.1–4.5 m bs; Fig. 2c). In places, the ice-rich diamicton shows deformation structures, such as recumbent isoclinal folds and boudinage structures, indicative of a strong linear shear stress and plastic deformation (Fritz et al., 2011). The massive ice below 6 m bs appeared whitish and was rich in spherical bubbles ca. 1 mm in diameter and in irregular distribution (Fig. 2d); fine dispersed mineral inclusions delineated subhorizontal layering. The massive ice was sampled at the

south-western margin of the thaw slump at a safely accessible site. The profile was horizontally cut by an electric chain saw (Stihl) across 0.8 m at about 7 m bs, totaling in five ice blocks. The five blocks are named as TSD19-02-06, TSD19-02-07, TSD19-02-08, TSD19-02-09 and TSD19-02-10, covering after cleaning the relative sampling widths of 0–12 cm, 14–29 cm, 30–43.5 cm, 45–57 cm and 59–72 cm, respectively (Fig. 2b). The ice was kept frozen upon return to the laboratory.

The HI19 ice was found at the headwall of a small active retrogressive thaw slump as a single ice wedge that was perpendicularly exposed across its growth direction over 1.6 m width (Figs. 1d and 3a, b). The overlying colluvium differentiated into (1) the 0.5-m-thick rooted active layer composed of modern vegetation and peat in the uppermost 0.15 m underlain by grey-brown sandy silts including peaty lenses up to 10 cm in diameter and pebbles 1–2 cm in diameter, and (2) the frozen 0.1-m-thick transient layer of the same composition as the active layer directly above the wedge ice, but showing cryostructures with ca. 1–2 mm wide and 1 cm long ice lenses in irregularly reticulated pattern. No recent ice-wedge growth has been observed in the frozen transient layer as rejuvenation veins were lacking and the polygonal structure was only slightly expressed at the surface. The wedge ice was foliated in 0.5–1 cm up to 1–2 cm wide vertical veins including rare organic and mineral material, and numerous spherical air bubbles 0.5–1 mm in diameter with no distinct distribution pattern, but also rare elongated bubbles 0.5 mm in diameter and up to 2–5 mm long. The ice wedge was horizontally cut by an electric chain saw (Stihl) across the entire exposed width at about 0.7 m bs totaling in ten blocks. Such near-surface sampling follows the recommendations by Campbell-Heaton et al. (2021a) as the stable isotope records might be less influenced by *in-situ* freezing and plugging. The ice was kept frozen upon return to the laboratory.

3.2. Stable-isotope analyses

Prior to analysis the sampled ice blocks were manually cleaned at −5 °C by scraping the outermost ~0.5 cm at each side of the blocks, and cut by band saw (Makita) mainly at 2-cm resolution resulting in 42
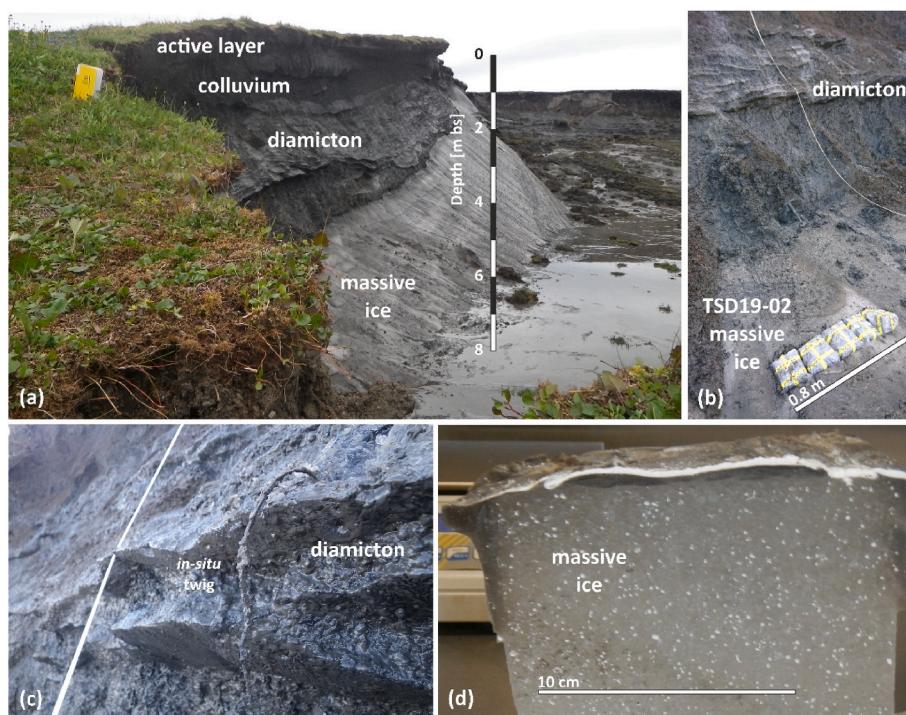
Fig. 2. Study site of the massive ice (TSD19-02) exposed in thaw slump D on Herschel Island showing (a) the general structure of the headwall, (b) the massive ice sampling transect over 0.8 m width in five blocks from left to right – TSD19-02-06 to TSD19-02-10, (c) close-up of *in-situ* twig found within the diamicton above the massive ice at 4.1 m bs, and (d) massive ice block sample (TSD19-02-06, representing 0–12 cm relative sampling width).
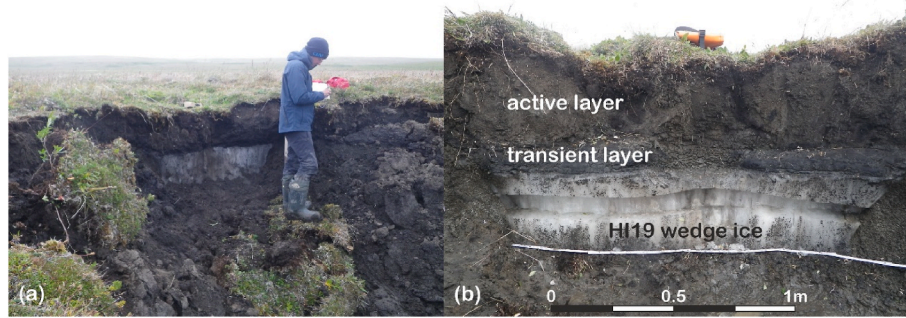
Fig. 3. Study site of the wedge ice (HI19) exposed in a small active thaw slump on Herschel Island showing (a) the headwall and (b) the wedge-ice sampling transect over 1.6 m width at 0.7 m bs.

samples from massive ice TSD19-02 and 67 samples from ice wedge HI19 (Appendix A). After melt, the samples were analyzed for oxygen (δ^{18}O) and hydrogen (δD) stable isotopes by a Finnigan MAT Delta-S mass spectrometer ($1\sigma < 0.1‰$ for δ^{18}O, $1\sigma < 0.8‰$ for δD; Meyer et al., 2000). The values are reported as per mil (‰) difference from the

VSMOW (Vienna Standard Mean Ocean Water). The deuterium excess (*d*) is calculated according to Dansgaard (1964) in Eq. (1):

$$d = \delta D - 8*\delta^{18}O \tag{1}$$

Additionally, archive data of massive-ice samples and wedge-ice

Table 1

Radiocarbon ages of plant macro-remains and DOC from host sediments, massive ice (MI, TSD19-02) and wedge ice (IW, HI19-01) of Herschel Island. n/a stands for not applicable. n/c stands for not calculated if ages were infinite or beyond the calibration limits (Reimer et al., 2020). Note that DOC ages were blank corrected. Results were rounded to the nearest 10 yr for samples with standard deviation in the radiocarbon age greater than 50 yr *DOC determinations from two ice samples (TSD19-06 and −07) which were combined in one DOC dating sample to ensure sufficient sample volume.

Sample type	Sample ID	Sampling depth	Relative position	Material	DOC	Sample weight after filtration	Lab ID	F^{14}C	Radiocarbon age	Calibrated 2σ age range	Calibrated median age
		[m bs]	[cm]		[mg L^{-1}]	[g]			[BP]	[cal BP]	[cal BP]
IW	HI19-01-02	0.7	7–26	DOC	1.77	51	7717.1.1	0.3842 ± 0.0103	7684 ± 213	8030–9010	8520
IW	HI19-01-03	0.7	32–41	DOC	4.92	118	7718.1.1	0.4089 ± 0.0110	7183 ± 213	7620–8390	8010
IW	HI19-01-04	0.7	52–60	DOC	2.68	120	7719.1.1	0.4535 ± 0.0105	6351 ± 185	6800–7580	7240
IW	HI19-01-05	0.7	72–80	DOC	4.99	113	7720.1.1	0.5267 ± 0.0108	5151 ± 163	5590–6280	5910
IW	HI19-01-06	0.7	85–98	DOC	7.15	139	7721.1.1	0.6677 ±0.0120	3245 ± 143	3080–3840	3470
IW	HI19-01-07	0.7	100–114	DOC	7.01	76	7722.1.1	0.5781 ± 0.0114	4402 ± 157	4580–5460	5040
IW	HI19-01-08	0.7	116–124	DOC	3.39	56	7723.1.1	0.4472 ± 0.0096	6465 ± 172	6990–7670	7360
IW	HI19-01-09	0.7	135–147	DOC	2.51	110	7724.1.1	0.3568 ± 0.0089	8279 ± 197	8600–9600	9220
IW	HI19-01-065-A	0.7	148	wood	n/a	n/a	5697.1.1	0.5398 ± 0.0023	4953 ± 35	5595–5840	5670
MI	TSD19-02-^{14}C-01-A	4.4	n/a	wood	n/a	n/a	5697.2.1	<0.0025	>47 990	n/c	n/c
MI	TSD19-02-^{14}C-01-B	4.4	n/a	wood	n/a	n/a	5698.1.1	<0.0025	>47 990	n/c	n/c
MI	TSD19-02-^{14}C-02	4.5	n/a	wood	n/a	n/a	5699.1.1	<0.0025	>47 990	n/c	n/c
MI	TSD19-02-^{14}C-A	4.1	n/a	wood	n/a	n/a	5699.2.1	<0.013	>53 460	n/c	n/c
MI	TSD19-02-^{14}C–B	4.1	n/a	wood	n/a	n/a	5699.3.1	<0.013	>53 460	n/c	n/c
MI	TSD19-02-^{14}C–C	4.1	n/a	wood	n/a	n/a	5699.4.1	<0.013	>53 460	n/c	n/c
MI	TSD19-02-^{14}C-D	4.1	n/a	wood	n/a	n/a	5700.1.1	<0.013	>53 460	n/c	n/c
MI	TSD19-02-06_07*	7	0–29	DOC	0.65/ 0.70	264	7725.1.1	0.0359 ± 0.0088	26 716 ± 1755	27 470–34 540	30 970
MI	TSD19-02-08	7	30–43.5	DOC	0.65	202	7726.1.1	0.0311 ± 0.0101	27 873 ± 2250	27 500–36 810	32 220
MI	TSD19-02-09	7	45–57	DOC	0.73	195	7727.1.1	0.0557 ± 0.0106	23 202 ± 1400	24 380–30 230	27 440
MI	TSD19-02-10	7	59–72	DOC	0.92	156	7728.1.1	0.0674 ± 0.0125	21 668 ± 1371	22 920–28 700	25 830

samples from Herschel Island as well as from the Yukon coast are considered in this study (Table 2; Fritz et al., 2011, 2015).

3.3. Dissolved organic carbon (DOC) analyses

A total of five samples from massive ice TSD19-02 (TSD19-02-06 to TSD19-02-10; Table 1) and eight samples from ice wedge HI19 (HI19-02 to HI19-09) were used for DOC content determinations across the respective horizontal sampling profiles at 10–15 cm resolution. Manually cleaned ice samples of 100–300 g were placed on an erected melt stand without any contact to plastic material and potentially contaminated margins were left to melt at room temperature for several hours and meltwater was discarded. The remaining clean ice blocks were thawed at room temperature overnight in pre-cleaned (purified water) glass beakers covered with pre-combusted (at 550 °C) aluminum foil. The meltwater was filtered within a glass filtration unit, equipped with pre-combusted glass fiber filters (Whatman GF/F; diameter: 47 mm, pore size: 0.7 μm) and acidified with HCl suprapur (30%) (between 50 and 200 μL) to pH < 2 in order to prevent microbial conversion. Values of pH were checked with glass sticks and pH paper while adding HCl to keep the added HCl to the required minimum. Samples were stored in acid-washed 250 ml HDPE bottles and frozen until further processing for radiocarbon dating and in 20 ml pre-combusted glass vials (unfrozen) for determination of DOC concentration. DOC concentrations (mg L^{-1}) were measured with a high-temperature (680 °C) combustion total organic carbon analyzer (Shimadzu TOC-VCPH). Internal acidification is used to convert inorganic carbon into CO_2, which is stripped out of solution. Non-purgeable organic carbon compounds are combusted and converted to CO_2 and measured by a non-dispersive infrared detector (NDIR). The device-specific detection limit is 0.4 μg L^{-1}. For each sample, one measurement with three to five repetitions was performed and results were averaged.

3.4. Radiocarbon dating

Radiocarbon analyses were performed on plant macro-remains (>1 mm) from host sediments and wedge ice, and on DOC from ice profiles to obtain age information of ground-ice formation (Table 1). The DOC ages integrate a certain profile width of <10–29 cm to ensure – depending on DOC concentrations – sufficient carbon content for radiocarbon measurements. Note, that after DOC analyses the neighboring samples TSD19-06 (0–12 cm relative sampling width) and TSD19-07 (14–29 cm relative sampling width) were further processed together to ensure sufficient sample material for DOC dating. In total, four DOC age determinations were obtained from profile TSD19 (Table 1). The radiocarbon analysis was performed at the MICADAS radiocarbon dating facility at AWI Bremerhaven, Germany. Details on sample preparation and laboratory procedures are given in Mollenhauer et al. (2021).

In total, one macro-remain sample was dated from the HI19 wedge ice and seven samples from the host deposits above the TSD19 massive ice. Plant remains were cleaned with acid-base-acid treatment (described in Mollenhauer et al., 2021) and subsequently combusted in an elemental analyzer (Elementar vario Isotope). Produced CO_2 was further graphitized utilizing the automated graphitization system (AGE-3; Ionplus AG; Wacker et al., 2010) and radiocarbon measurements were conducted. Radiocarbon data were normalized and blank corrected against size-matched standard (NIST Oxalic Acid II, NIST SRM4990C) and ^{14}C-free blank material (Phthalic Acid; Sigma Aldrich 320064), and data integrity was checked against the processing wood standard IAEA-C5.

DOC sample volumes containing ∼90 μgC were transferred to pre-combusted 100 mL glass pear-shaped flask and the water was dried by rotary evaporation. The residual organic carbon was transferred into 50 μl tin liquid capsules and dried again for 2 days inside an evacuated desiccator at 40 °C. Radiocarbon analyses were carried out with the EA-GIS-AMS setup following established standard operation procedures as

Table 2

Stable isotope (δ18O, δD and deuterium excess) minimum (min), mean, maximum (max) values, standard deviation (SD), and number of samples (n), slope, intercept and coefficient of determination (r^2) from wedge ice (WI) and massive ice (MI) on Herschel Island. The 2019 dataset is given in Appendix A. *Literature data of massive ice from Fritz et al. (2011).

Ground ice type (year of sampling)	Sample ID	δ18O [‰] vs. SMOW				δD [‰] vs. SMOW				Deuterium excess [‰] vs. SMOW				n	Slope	Inter- cept	r^2
		MIN	MEAN	MAX	SD	MIN	MEAN	MAX	SD	MIN	MEAN	MAX	SD				
WI (2019)	HI19	−20.52	−18.40	−16.02	1.14	−156.2	−138.4	−118.4	9.3	5.77	8.76	11.07	1.38	67	8.01	9.05	0.98
MI (2019)	TSD19–02	−33.48	−33.19	−32.57	0.30	−259.9	−257.6	−253.0	2.2	6.85	7.94	8.93	0.46	42	6.97	−26.11	0.97
MI (2009)	TSD09-5*	−33.70	−32.98	−32.19	0.46	−261.4	−256.7	−250.9	3.1	6.31	7.14	8.18	0.69	9	6.77	−33.49	0.98
MI (2008)	TSD-DOME*	−33.78	−32.71	−31.26	0.78	−262.4	−255.1	−243.7	5.7	5.26	6.65	8.46	0.87	19	7.26	−17.60	0.99
MI (2006)	TSD-MI*	−34.19	−33.34	−32.49	0.63	−264.7	−258.7	−252.4	4.6	6.59	8.00	9.29	0.86	12	7.15	−20.22	0.98
MI (2006–2019)	all TSD records	−34.19	−33.08	−31.26	0.56	−264.7	−257.1	−243.7	3.9	5.26	7.56	9.29	0.86	82	6.89	−29.27	0.98

outlined in Mollenhauer et al. (2021). Radiocarbon data were normalized and blank corrected against standard (NIST Oxalic Acid II; NIST SRM4990C) and blank (^{14}C free) CO_2 gas. Further, the tin capsule blank was determined and corrected for following the protocol described by Sun et al. (2020).

All radiocarbon results were reported as $F^{14}C$ and conventional radiocarbon ages. We used the IntCal20 dataset (Reimer et al., 2020) to calibrate the ages with CALIB Radiocarbon Calibration version 8.2 including literature data, which are given as calibrated years before present (cal BP).

4. Results

4.1. Stable water isotope composition of ground ice

The stable water isotope composition of the massive ice TSD19–02 exhibits mean values of -33.2 ± 0.3‰ in $\delta^{18}O$, of -258 ± 2‰ in δD and of 7.9 ± 0.5‰ in d (Table 2). The isotope data group below the Global Meteoric Water Line (GMWL; Craig, 1961) and the closest modern Local Meteoric Water Line (Inuvik LMWL; Fritz et al., 2022) at a slope of 7 and an intercept of -26.1 (Fig. 4a). The isotope data show only minimal variations of about 0.9‰ in $\delta^{18}O$, 7‰ in δD, and 2‰ in d. The TSD19-02 sampling transect shows no distinct pattern except for a shift of about 0.5‰ in $\delta^{18}O$ at 59 cm sampling width (Fig. 5a).

The stable water isotope composition of the wedge ice HI19 is characterized by mean values of $\delta^{18}O$ of -18.4 ± 1.1‰, δD of -138 ± 9‰ and d of 8.8 ± 1.4‰ (Table 2). The data mostly group along or slightly below the GMWL and clearly above the modern Inuvik LMWL at a slope of 8 and an intercept of 9.1 (Fig. 4b). The isotope data show variations of about 4.5‰ in $\delta^{18}O$, 37‰ in δD, and 5‰ in d. The horizontal HI19 sampling transect across the growth direction of the wedge ice resembles some symmetric pattern with lowest $\delta^{18}O$ and d values at 85–90 cm sampling width (Fig. 5b).

4.2. Dissolved organic carbon (DOC) content of ground ice

The **TSD19** massive ice exhibits distinctly lower DOC concentrations when compared to the HI19 wedge ice with a mean of 0.7 ± 0.1 mg L^{-1}. The profile shows a slight increasing trend from 0.7 to 0.9 mg L^{-1} between 0-29 cm and 59–72 cm relative sampling width, respectively (Fig. 5a).

The DOC concentration of the **HI19** wedge-ice profile shows variations between 1.8 and 7.2 mg L^{-1} at a mean value of 4.3 ± 2.1 mg L^{-1}. There is no trend or symmetry on DOC concentrations seen in the profile although highest values of >7 mg L^{-1} occur close to the central part of the profile between 85 and 114 cm relative sampling width (Fig. 5b).

4.3. Radiocarbon ages

The four DOC ages from the TSD19–02 massive ice span from 32 220 to 25 830 cal BP (Fig. 5a), while dating of *in-situ* found wood remains from the diamicton overlying the massive ice at sampling depths between 4.5 and 4.1 m bs produced in total seven infinite ages of >53 460 and > 47 990 BP (Table 1).

In total, eight DOC radiocarbon ages were obtained across the ice-wedge profile HI19. The youngest DOC age of 3470 cal BP was found in the central part at 85–98 cm relative sampling width, while towards the profile margins in both direction the ages become consecutively older reaching 8520 cal BP at 7–26 cm and 9220 cal BP at 135–147 cm relative sampling width (Fig. 5b). Additionally, one age on wood found enclosed within the wedge ice at its margin at 148 cm relative sampling width revealed an age of 5670 cal BP.
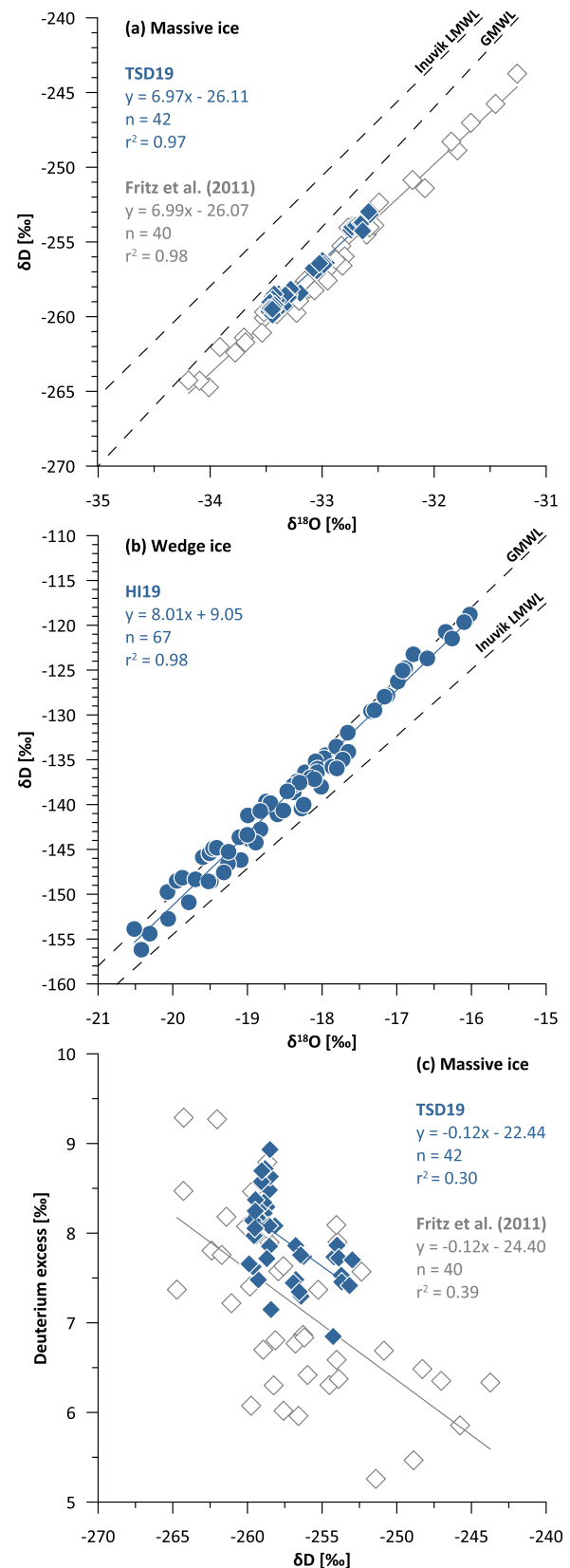
Fig. 4. Stable-water-isotope composition ($\delta^{18}O$, δD) of (a) massive ice including literature data from Fritz et al. (2011) and (b) wedge ice on Herschel Island. The relationship of δD and deuterium excess for the massive ice is given in (c). The Inuvik Local Meteoric Water Line (LMWL) refers to Fritz et al. (2022) and the Global Meteoric Water Line (GMWL) to Craig (1961).
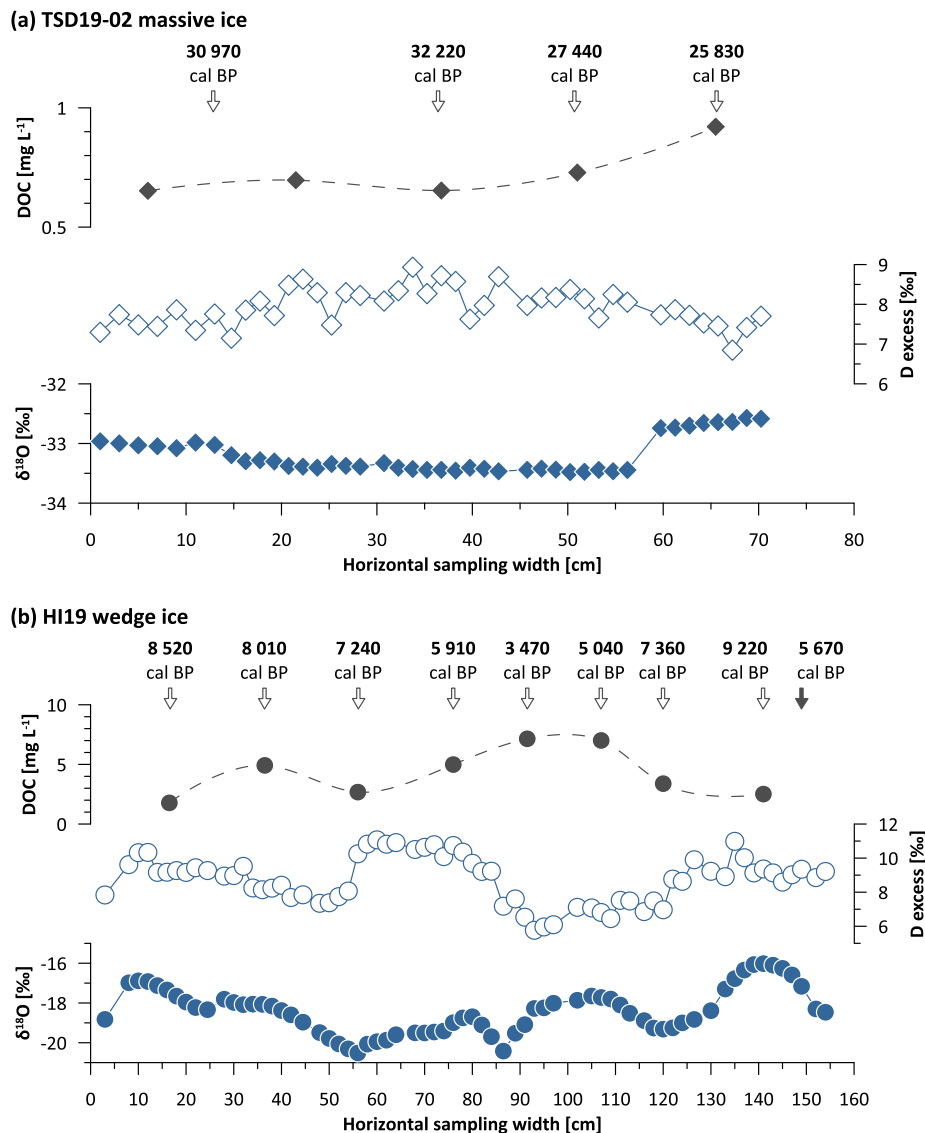
Fig. 5. Sampling profiles of (a) the HI19 wedge ice and (b) the TSD19-02 massive ice showing δ18O values, Deuterium excess values and DOC concentrations. Additionally, radiocarbon ages are indicated above the DOC curves by white arrows for DOC-derived ages and by a grey arrow for the single plant macrofossil age from HI19 (Table 1).

5. Discussion

5.1. Ground ice properties on Herschel Island (Qikiqtaruk)

5.1.1. Massive-ice stable isotopes and DOC

The stable isotope composition of the massive ice sampled in 2019 with mean values of -33.2 ± 0.3‰ in $\delta^{18}O$, of -258 ± 2‰ in δD and *d* of 7.9 ± 0.5‰ (Fig. 4a) fits into the range of previously obtained data of this massive ice with mean values between -33.3 ± 0.6‰ and -32.7 ± 0.8‰ in $\delta^{18}O$, -259 ± 5 and -255 ± 6‰ in δD, and between 6.7 ± 0.9 and 8.0 ± 0.9‰ in *d* (Table 2; Fig. 6; Fritz et al., 2011, 2015). Michel (1990) presented similar isotopic signatures of the massive ice on Herschel Island with values from -35 to -27‰ in $\delta^{18}O$ and -265 to -210‰ in δD that define a wider range of the isotopic composition of the Herschel massive ice. The latter study presents also regional isotopic composition data of massive ground ice at Peninsula Point, Sabine Point and Kay Point that all resemble the Herschel massive ice, pointing to similar origin and preservation conditions.

The very low $\delta^{18}O$ and δD values of the Herschel massive ice suggest a glacial origin of the massive ice that has survived the last deglaciation.

The obtained DOC radiocarbon ages (32 220 to 25 830 cal BP) point to ice formation during the Late Wisconsin full glacial including the Last Glacial Maximum (LGM). The isotopic composition of the Herschel massive ice is further in line with those of other late Pleistocene buried ice from the LIS margins such as from the relatively nearby sites on the Peel Plateau (Lacelle et al., 2018) and Richards Island (Dallimore and Wolfe, 1988), Victoria Island (Lorrain and Demeur, 1985) and from the more distant Bylot Island (Coulombe et al., 2019). Both the δD-$\delta^{18}O$ slope of 6.97 and *d*-δD slope of -0.12 of the 2019 Herschel massive ice samples (Fig. 4c) are very similar to those of the Peel Plateau massive ice (6.35 and -0.22, respectively), which is interpreted as buried glacier ice (Lacelle et al., 2018). Furthermore, they are close to those of modern precipitation at Inuvik (7.39 and -0.07, respectively, Fritz et al., 2022) suggesting that the Herschel massive ice was formed from meteoric water, as glacier ice fed by atmospheric precipitation. However, solely based on the existing stable isotope evidence, freezing of glacial melt-water under non-equilibrium conditions cannot be excluded (Fritz et al., 2011). Additional support for a glacier ice origin comes from the white appearance of the ice and from the richness and irregular distribution of spherical air bubbles which is typical for buried englacial ice (Coulombe
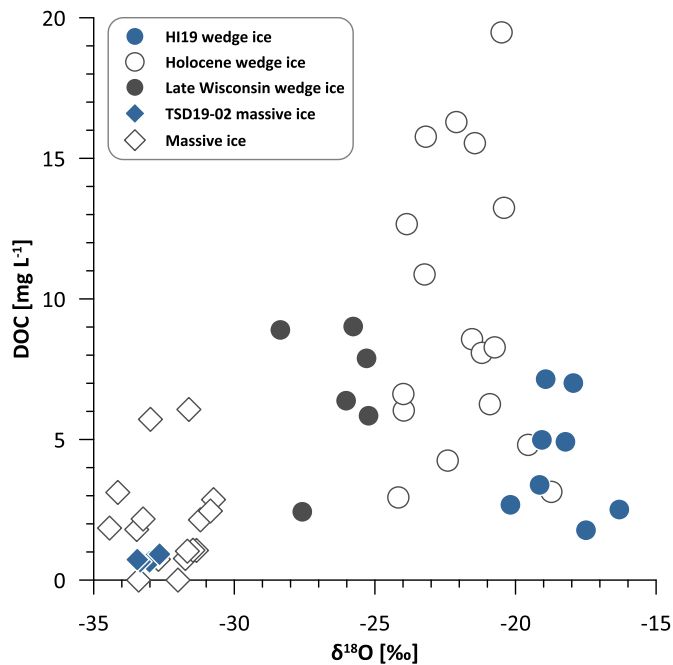
Fig. 6. $\delta^{18}O$ and DOC values of different ice types and among ice wedges of different age on Herschel Island and the Yukon coast showing data from this study and Fritz et al. (2015).

et al., 2019).

The DOC concentrations of the Herschel massive ice are generally low with a mean of 0.7 ± 0.1 mg L^{-1} (Fig. 6) and largely resemble previous records from massive ice of Kay Point (on the Yukon mainland coast) and Herschel Island ranging from below detection limit to 6.1 mg L^{-1} (mean 1.7 mg L^{-1}; Fritz et al., 2015; Tanski et al., 2016). DOC concentrations from glacial ice corresponding to the ice sheet that probably contributed to the Herschel massive ice have – to our knowledge – not been reported. Glacial ice from the Canadian Arctic sampled on Axel Heiberg and Ellesmere islands at depths down to about 13 m below surface (Pautler et al., 2012) exhibits DOC concentrations between 0.4 and 1.1 mg L^{-1}, framing the DOC concentrations of the Herschel massive ice. For glacial ice that has been buried after deglaciation, the detected low DOC has atmospheric origin from eolian organic carbon (OC) deposition onto the snow, firn or ice (Tanski et al., 2016). In contrast, the incorporation of sedimentary OC from the underlying glacial bed by melt and refreeze (basal regelation ice) into the massive ice would potentially produce higher DOC concentrations and make any age interpretation of DOC highly complicated as OC could pre-date glaciation and be of any age. However, terrestrial ground ice that has been in contact with soil and vegetation (i.e., ice wedges, pore ice) commonly shows much higher DOC concentrations (Fig. 6) as carbon is leached from the surface and the host deposits (e.g., Guo and Macdonald, 2006).

Moorman et al. (1996) argues that the gas, its CO_2 contents and $\delta^{13}C$ values indicate the ice bodies studied also on Herschel Island were not formed directly from the compaction of snow and states that "*the origin of the [...] samples is not definite, except that they are likely not of a 'firn' ice origin.*". However both, CO_2 and $\delta^{13}C$ from gas inclusions, may be influenced by post-depositional microbial activity in a permafrost environment and may hence not be conclusive to assess the formation conditions of the massive ice.

Given the very negative stable isotope composition of the massive ice on Herschel Island, the numerous spherical air bubbles, its very low DOC content that largely excludes terrestrial carbon sources and the rather young DOC ages that make the incorporation of old OC unlikely, we conclude a massive ice genesis on Herschel Island rather as buried glacier ice than as basal regelation ice.

5.1.2. Wedge-ice stable isotopes and DOC

Stable isotope analyses of wedge ice from the Beaufort Sea coastal region including Herschel Island exhibit a consistent pattern that differentiates into generations of Holocene and truncated Late Wisconsin ice wedges, both with distinct isotopic compositions. Michel (1990) reported $\delta^{18}O$ values for younger (presumably Holocene) ice wedges in the Beaufort Sea coastal region ranging from -26 to -21‰ (mean value for an Herschel Island ice wedge of -22‰) and noted explicitly that small epigenetic ice wedges up to 0.5 m width on Herschel Island yield -20 to -17.5‰. Truncated ice wedges of presumably Late Wisconsin age show more depleted $\delta^{18}O$ values between -33 and -27‰ (Michel, 1990). Similar isotopic compositions from Herschel Island are given in Fritz et al. (2012) with $\delta^{18}O$ mean of -22.1‰, δD mean of -167‰ and d mean of 9.7‰ of Holocene wedge ice, while Late Wisconsin ice wedges show a $\delta^{18}O$ mean of -29.1‰, δD mean of -232‰ and d mean of 0.1‰ (Fig. 6). Thus, the present record from HI19 wedge ice fits isotopically into the previous Holocene records, and adds valuable age information on postglacial polygon formation by direct dating between 9220 and 3470 cal BP.

Similar DOC concentrations with overlap in Late Wisconsin and Holocene ice wedges along the Yukon Coast (Fig. 6) suggests that OC sequestration into wedge ice was similarly effective during both periods although the carbon sources might have been different. Generally, DOC of ice wedges is mainly derived from tundra surface OC when snow melt leaches DOC from particulate OC and then gets transported into the frost crack. Other DOC sources can be windblown OC onto the snowpack and OC within the contraction crack itself. The similar DOC concentrations in Late Wisconsin and Holocene Herschel wedge ice on Herschel Island are in contrast to findings of a pan-arctic study of Fritz et al. (2015), who found higher DOC concentrations in ice wedges from the late Pleistocene compared to the Holocene. On a pan-arctic scale this was explained by rapid sediment and OC accumulation, the prevalence of more easily degradable vegetation and immediate incorporation into permafrost. This may hold true for syngenetic ice wedges in previously unglaciated regions such as in Beringia. Syngenetic ice wedges formed during periods of rapid sedimentation, where ice wedge growth and deposition occurred simultaneously, for example in late Pleistocene Yedoma Ice Complex deposits (Schirrmeister et al., 2013). If compared to DOC concentrations obtained from Tuktoyaktuk Holocene wedge ice (ca. 4–7 ppm [mg L^{-1}], Holland et al., 2020), the Herschel Island record of HI19 shows lower values ranging from 1.8 to 7.2 mg L^{-1}.

Epigenetic ice wedges dominate on Herschel Island. They have formed post-depositionally on a pre-existing landscape. Even Late Wisconsin ice wedges on Herschel Island must postdate the formation of the island itself as a push moraine. After the LIS retreat, frostcracking and ice-wedge development probably started in a barren landscape with sparse vegetation cover (Fritz et al., 2012). Low organic carbon availability on the surface may have led to relatively low DOC concentrations of <10 mg L^{-1} in Late Wisconsin wedge ice along the previously glaciated part of the Yukon Coast. Sedimentary carbon could have been one of the DOC sources for Late Wisconsin ice wedges as their ice is mostly milky and brownish with considerable sediment admixtures. With vegetation succession and polygonal peatland development during the Holocene (Fritz et al., 2016), the organic carbon availability from surface litter increased and is reflected in maximum DOC concentrations of up to 20 mg L^{-1} (Fig. 6). DOC sequestration into ground ice is a complex process that is dependent on water sources, freezing processes, active-layer properties, vegetation cover and communities, deposition rates, and the inorganic geochemical signature of the ambient water to form ground ice (Fritz et al., 2015).

The newly studied Holocene wedge ice of HI19 provides a characteristic stable isotope and DOC signature of such ground ice on Herschel Island, and for the first time a conclusive and continuous directly dated age record of ice-wedge growth between 9220 and 3470 cal BP.

5.2. Landscape evolution on Herschel Island (Qikiqtaruk) in regional context

The ground-ice inventory of Herschel Island is extraordinarily diverse, comprising glacial and periglacial formations and allowing for insights into the glacial and postglacial landscape evolution (Fritz et al., 2012). Ongoing research provides new data on ground-ice properties and age determinations, which sharpen our understanding of regional-scale extrinsic (including climate dynamics, marine transgression, postglacial isostatic uplift) and landscape-scale intrinsic (including hydrology, relief, sediment properties) forcings that defined the geomorphodynamics on local scale. In this respect, Herschel Island provides an ideal playground to delineate the interaction of multiple drivers that shaped over time the modern appearance of the island, and to deduce the larger context of natural history in the Western Canadian Arctic.

The newly obtained age information from the massive ice points to ice formation during the Late Wisconsin full glacial while the infinite ages of >53 460 and > 47 990 BP from plant macro-fossils (woody remains) of the diamicton topping the massive ice most likely originate from relocated material thrusted and pushed by the glacial advance. Zazula et al. (2009) discuss the origin of infinite dated organic material (providing ages beyond the range of radiocarbon dating) on Herschel Island from terrestrial surfaces of the exposed Beaufort Shelf, which was included into Herschel Island deposits as a result of ice-thrust. Previous attempts to directly date the massive ice revealed a single CO_2-derived radiocarbon age of 21 290 cal BP (17 570 ± 300 BP) from air inclusions of the massive ice sampled about 2 km NE of profile TSD19-02 at the Thetis Bay coast (Moorman et al., 1996). As massive ice DOC is not necessarily composed of only "fresh" carbon but might include portions of "older" carbon (Lachniet et al., 2012), we regard our DOC ages between about 32 220 and 25 830 cal BP as maximum ages and assume that the youngest measured age (25 830 cal BP) is closest to the true formation age of the buried glacier ice. Thus, the age of the massive ice on Herschel Island dated by two independent approaches confirms its formation during the LGM (Fig. 7). This is in line with assumptions of Lacelle et al. (2018) for the age of buried ice of the LIS in this region considering the transport time from the ice sheet accumulation center to the margin. Our dating results for the buried glacier ice make plausible the absence of vertebrate fossils on today's Herschel Island between 41 190 and 21 120 cal BP (between 36 160 ± 530 and 17 490 ± 90, respectively; Zazula et al., 2009).

The mechanism of massive-ice formation or preservation at the LIS marginal regions is still discussed either as regelation ice (Rampton, 1991), segregation-injection ice (French and Harry, 1990) or buried glacial ice (Coulombe et al., 2019). For the Herschel Island massive ice, no evidence of closed-system freezing, no vertical pattern in stable isotopes and no distinct negative δD-d slopes have been observed yet (Fritz et al., 2011) to conclude its genesis as massive segregated ice. Furthermore, the huge extent of the massive ice on the island would have needed an enormous freshwater source within the fine-grained diamicton of marine origin to facilitate open-system freezing of segregated-intrusive ice. It would be further expected to form segregated-intrusive ice along zones of weakness that would result in rather complicated structures and not such extensive homogenous lateral horizontal bedding as seen in the massive ice. Even ice diapirs that are formed by density inversions of the overlying material which is not equally thick along the strong geomorphic gradients of the end moraine landscape are always related to the main ice body.

The formation maximum age of Herschel Island as ice-thrust moraine and the respective timing of the maximum extent of the LIS along the Yukon Coastal Plain is yet based on the youngest radiocarbon date of 15 990 cal BP (13 300 ± 70 Fritz et al., 2012) obtained so far from the diamicton covering the massive ice on the island (Fig. 7). This interpretation assumes that the dated plant material accumulated prior to the glaciotectonic deformation. As glaciotectonism deformed both the diamicton and the underlying massive ice, the formation age of the latter – spanning from at least 32 220 to 25 830 cal BP – is in line with such interpretation. Further evidence for the timing of the LIS maximum extent forming the Herschel Island ice-thrust ridge (or in other words the minimum age for its deglaciation) might be deduced from a probably *in-situ* collected horse cranium (*Equus lambei*; Harington, 1989; 2003 cited in Zazula et al., 2009) dated to 20 170 and 19 550 cal BP (to 16 700 ± 200 and 16 200 ± 150 BP, respectively; Fig. 7).

An increasing number of studies conclude that the maximum extent of the LIS during the late Pleistocene reached its northwestern position during the Late Wisconsin. The position of retrogressive thaw slumps in the region formed by melting massive ice might be indicative (Fig. 1a). A relatively short-lived regional Late Wisconsin ice advance between about 22 and 15 cal ka BP followed by ice sheet recession since around 14 cal ka BP at the latest was found for the Tuktoyaktuk Coastlands (Mackay and Dallimore, 1992; Bateman and Murton, 2006; Murton et al., 2007), Banks Island (England et al., 2009), the Peel Plateau and Richards Island (Lacelle et al., 2018), and the Richardson and Mackenzie mountains (Kennedy et al., 2010). On the Tuktoyaktuk Coastlands sands of the Kittigazuit Formation (dunes) were overridden by glacier ice, which deposited a till (Murton et al., 2007). Luminescence dating of the dune sands suggests that the glaciation probably occurred no earlier than 22 ka and possibly as late as 16 ka (Bateman and Murton, 2006; Murton et al., 2007). Deglaciation of the Tuktoyaktuk Coastlands had commenced by 14 300 cal BP, based on radiocarbon ages from organic material of lacustrine basal deposits and from infrared-stimulated luminescence (IRSL) ages from sand wedges (Ritchie, 1984; Murton et al., 1997). Glacial ice deposited a widespread till and caused ice thrusting near its margin (Rampton, 1982, 1988). Glacial overriding of permafrost caused deformation of pre-existing massive ice (Rampton and Mackay, 1971), burial of basal ice by glacier thrusting of permafrost deposits, and emplacement of a glacitectonite (Murton et al., 2005; Fritz et al., 2012). On southern Melville Island, radiocarbon dates of ice-transported marine molluscs within the most extensive Laurentide
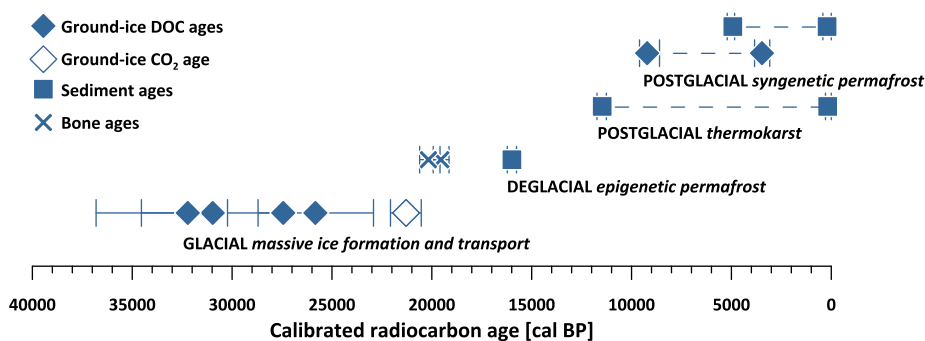
Fig. 7. Summary plot of radiocarbon ages obtained on Herschel Island delineating its Late Wisconsin to Holocene landscape evolution. Data derive from (1) this study (ground-ice DOC ages; Table 1), (2) Moorman et al. (1996; CO_2 age of the massive ice), (3) Fritz et al. (2012; youngest sediment age below thaw unconformity in epigenetically frozen diamicton), (4) Harington (1989, 2003 cited in Zazula et al., 2009; presumably *in-situ* horse bone ages), (5) Fritz et al. (2016; syngenetically frozen polygon deposits), and (6) Lenz et al. (2013; thermokarst lake deposits). Symbols indicate the median calibrated ages, and error bars the calibrated 2σ age ranges. Note that only oldest to youngest ages of respective postglacial profiles are shown (connected by dotted lines).

till yielded ages spanning 49 to 25 ka BP (England et al., 2009), thus providing a minimum age for glaciation. Lacelle et al. (2018) argued that buried ice from the LIS in northwestern Canada was stranded or buried shortly after the LIS reached its maximum extent at about 21–17 ka BP, with the LIS receding by 14–10 ka BP from LIS marginal regions such as the Peel Plateau, Richards Island, Victoria Island, and Bylot Island.

Our direct dating of buried glacier ice by DOC radiocarbon dating provides further independent evidence about the timing of advance and retreat of the LIS. The direct ages provide a maximum age for the ice advance that took place after 25 830 cal BP according to the DOC age of our study or at least after 21 290 cal BP according to the CO_2 age by Moorman et al. (1996). There is time needed to transport the ice from the accumulation center to the margin where it got buried. The ice is apparently of LGM-age and originated from either the Keewatin or the Plains ice divide (Lacelle et al., 2018), both having a distance from Herschel Island of a 1000 km or more.

Late Wisconsin permafrost aggradation and polygon formation on Herschel Island as reflected by truncated and epigenetic ice wedges occurred prior to 11 250 cal BP (9840 $\pm$ 60; Fritz et al., 2012), and took place simultaneously with extensive late glacial ice-wedge development prior to the end of the Younger Dryas cold interval as recorded in the Barrow region, northern Alaska (Meyer et al., 2010).

Traces of the subsequent early Holocene warming are found in the sedimentary records on Herschel Island as pronounced thaw unconformity in permafrost deposits truncating the Late Wisconsin ice wedges (Fritz et al., 2012). The youngest age from below the thaw unconformity dates to 15 990 cal BP (13 300 $\pm$ 70 BP) and the oldest age from above the thaw unconformity to 11 850 cal BP (10 190 $\pm$ 50 BP; Fritz et al., 2012). Further evidence is found in the basal age of Lake Herschel that developed after initial thaw subsidence and melt-out of ground ice as thermokarst lake since about 11 470 cal BP (9990 $\pm$ 60 BP; Lenz et al., 2013; Fritz et al., 2018).

Continuous polygon formation in a drained thermokarst basin since about 4000 cal BP was deduced from a permafrost core obtained on Herschel Island (Fritz et al., 2016) only about 300 m NE of the sampling location of HI19. Pre-dating ice-wedge growth and thus polygon formation since the early mid-Holocene between 9220 and 3470 cal BP is seen in the DOC-based chronology from the HI19 record. As towards the profile margins the DOC ages of HI19 become consecutively older in both directions, regular growth directions with active frost-cracking near the center seems likely that produced a quasi-symmetry in the DOC-based chronology (Fig. 5b). However, the marginal plant macro-fossil age of 5670 cal BP might point to secondary cracking as deviations in the symmetry of the age marks occur when cracking not necessarily takes place strictly in the middle of the ice wedge, but in arbitrary cross-sections. There may have been more or less constant cracking zones at certain time intervals, the position of which varied over time.

If compared to regionally available directly dated Holocene ice-wedge records from the Tuktoyaktuk coastlands (Holland et al., 2020), inconsistencies with the Herschel record are obvious. Generally, the Herschel records are less depleted by 5–6‰ than those from the Tuktoyaktuk coastlands (mean $\delta^{18}O$ of -24.1‰; Holland et al., 2020). This applies not only to the HI19 ice wedge (mean $\delta^{18}O$ of -18.4 ± 1.1‰), but also to previously studied Holocene wedge ice on Herschel (mean $\delta^{18}O$ of -22.1‰; Fritz et al., 2012). All datasets show similar mean d excess values and slopes of 8.8‰ and 8.01 for HI19, 9.7‰ and 7.7 in Fritz et al. (2012) and 9.5‰ and slopes between 6.51 and 7.85 in Holland et al. (2020), indicating that the differences in $\delta^{18}O$ do not originate from post-depositional fractionation. In contrast, different pathways of precipitation-bearing air masses could have an impact. Assuming the main moisture source in the North Pacific and adjacent seas, the more eastern location of the Tuktoyaktuk coastlands would result in a longer distillation path of moisture and, hence, a more depleted isotopic composition. Additionally, a different proportion of isotopically depleted Mackenzie River water (compared to seawater) as

secondary regional moisture source during the shoulder seasons could lead to such differing isotope patterns. Nevertheless, the HI19 ice wedge is particularly enriched - even in comparison to the Holocene ice wedges studied by Fritz et al. (2012) and also more enriched than modern ice wedges in this region (Michel, 1990).

While the Holland et al. (2020) record of Holocene wedge ice spans the time period from about 7400–640 years b2k, the HI119 ice wedge dataset covers the period between about 9220 and 3470 cal BP, thus missing much of the Late Holocene represented in the Holland et al. (2020) dataset. When using the combined age-isotope information of our directly dated samples, a winter cooling trend toward the mid-Holocene can be observed until about 7240 cal BP (Fig. 5b), the period largely not covered by the Tuktoyaktuk dataset (Holland et al., 2020). For the overlap period of the Tuktoyaktuk and the Herschel records, the latter does not show any clear trend but consists only of three data points between 5910 and 3470 cal BP which can hardly be interpreted in a meaningful way.

Little is known about the cold-season climate development of East Beringia during the early Holocene. According to Kaufman et al. (2004) the Holocene Thermal Optimum (HTM) in the region has occurred between ca. 11 and 8 cal BP. Hence, a cooling towards the mid-Holocene as seen in the HI19 data seems reasonable, even though most available records rather attribute the post-HTM cooling to the warm season while the winter temperatures over this period are not constrained yet.

In recent times, no active ice-wedge polygon formation seems to be taking place on Herschel Island as also the studied HI19 exposure lacks recent ice veins in the transient layer and no distinct pattern of evolving low-center polygons is expressed at the surface. If present, the surface on the island exhibits largely degrading features such as high-center polygons while on the Yukon Coastal Plain low-center polygons indicating active ice-wedge growth are present (Fritz et al., 2016).

6. Conclusions

Our study of glacial and periglacial ground ice on Herschel Island discusses newly obtained data on the geochemical properties and formation ages of Late Wisconsin massive ice and Holocene wedge ice. The ice bodies were directly dated by DOC radiocarbon dating and yield thus evidence for the timing of their respective formation. Complementing previous research, the present study provides arguments for the hypothesis of a glacial origin of the massive ground ice exposed in retrogressive thaw slumps on Herschel Island. These arguments include very low stable isotope values, low DOC contents and shape, number and distribution of air bubbles. DOC radiocarbon dating shows that the massive ice formed in Late Wisconsin and thus rejects earlier hypotheses about its origin in Early Wisconsin time. The Late Wisconsin glacial ice that substantially builds-up the modern Herschel Island was moved, glaciotectonically deformed and buried during the last advance of the Laurentide Ice Sheet.

The postglacial landscape evolution during the Holocene was characterized by syngenetic ice-wedge polygon formation in aggrading permafrost. The present records confirm ice-wedge growth between 9220 and 3470 cal BP, while Holocene polygon formation since about 4000 cal BP has been deduced from sedimentary records. However, recent ice-wedge growth has not been observed and polygon patterns in the modern surface show degradation stages such as high-center polygons.

The postglacial landscape evolution on Herschel Island is largely determined by the wide presence of massive ice whose preservation and ongoing destruction controls surface and relief-shaping processes. Its origin as buried glacial ice sheds light on the interplay of glacial and periglacial processes superimposed by climate control during deglaciation and afterwards. Further research might address obtaining more insights into ice-sheet dynamics prior to deglaciation in context of the distribution of glacial remnants elsewhere in the region.

Funding

Author contributions

SW and MF designed the study and conducted the fieldwork. TO supported the cold-lab work and provided expertise in stable-isotope interpretation. AIK provided expertise on RTS processes and designed Fig. 1. GM and HG performed radiocarbon dating at the MICADAS facility. All authors contributed to the interpretation and discussion, and the final draft of the manuscript.

Declaration of competing interest

The authors declare that they have no known competing financial interests or personal relationships that could have appeared to influence the work reported in this paper.

Data availability

All original data of this study are included in the paper in tables 1 and 2, and in Appendix A.

Acknowledgements

Appendix A. Supplementary data

Supplementary data to this article can be found online at https://doi.org/10.1016/j.qsa.2023.100077.

References

Ashastina, K., Kuzmina, S., Rudaya, N., Troeva, E., Schoch, W.H., Römermann, C., Reinecke, J., Otte, V., Savvinov, G., Wesche, K., Kienast, F., 2018. Woodlands and steppes: Pleistocene vegetation in Yakutia's most continental part recorded in the Batagay permafrost sequence. Quat. Sci. Rev. 196, 38–61. https://doi.org/10.1016/j.quascirev.2018.07.032.

Bateman, M.D., Murton, J.B., 2006. Late Pleistocene glacial and periglacial aeolian activity in the Tuktoyaktuk Coastlands, NWT, Canada. Quat. Sci. Rev. 25, 2552–2568. https://doi.org/10.1016/j.quascirev.2005.07.023.

Burn, C.R., 2012. Permafrost. In: Burn, C.R. (Ed.), Herschel Island Qikiqtaryuk: A Natural and Cultural History of Yukon's Arctic Island. University of Calgary Press, Calgary, pp. 65–77.

Burn, C.R., Zhang, Y., 2009. Permafrost and climate change at Herschel island (qikiqtaruq), Yukon territory, Canada. J. Geophys. Res. – Earth Surf. 114, F02001 https://doi.org/10.1029/2008JF001087.

Campbell-Heaton, K., Lacelle, D., Fisher, D., 2021a. Ice wedges as winter temperature proxy: principles, limitations and noise in the δ18O records (an example from high Arctic Canada). Quat. Sci. Rev. 269, 107135 https://doi.org/10.1016/j.quascirev.2021.107135.

Campbell-Heaton, K., Lacelle, D., Fisher, D., Pollard, W., 2021b. Holocene ice wedge formation in the eureka sound lowlands, high arctic Canada. Quat. Res. 102, 175–187. https://doi.org/10.1017/qua.2020.126.

Coulombe, S., Fortier, D., Lacelle, D., Kanevskiy, M., Shur, Y., 2019. Origin, burial and preservation of late Pleistocene-age glacier ice in Arctic permafrost (Bylot Island, NU, Canada). Cryosphere 13, 97–111. https://doi.org/10.5194/tc-13-97-2019.

Couture, N., 2010. *Fluxes of Soil Organic Carbon from Eroding Permafrost Coasts, Canadian Beaufort Sea*. PhD Thesis. Department of Geography, McGill University, Montreal, p. 155.

Craig, H., 1961. Isotopic variations in meteoric waters. Science 133, 1702–1703. https://doi.org/10.1126/science.133.3465.1702.

Dallimore, S.R., Wolfe, S.A., 1988. Massive ground ice associated with glaciofluvial sediments, Richards Island, N.W.T., Canada. In: Senneset, K. (Ed.), Proceedings of the Fifth International Permafrost Conference, vol. 1. Tapir Publishers, Trondheim, Norway, pp. 132–137.

Dalton, A.S., Stokes, C.R., Batchelor, C.L., 2022. Evolution of the Laurentide and Innuitian ice sheets prior to the Last Glacial Maximum (115 ka to 25 ka). Earth Sci. Rev. 224, 103875. https://doi.org/10.1016/j.earscirev.2021.103875.

Dansgaard, W., 1964. Stable isotopes in precipitation. Tellus 16 (4), 436–468. https://doi.org/10.3402/tellusa.v16i4.8993.

Dubikov, G.I., 2002. Composition and Cryogenic Structure of the Western Siberia Permafrost, second ed. GEOS, Moscow (in Russian).

England, J.H., Furze, M.F.A., Doupé, J.P., 2009. Revision of the NW Laurentide ice sheet: implications for paleoclimate, the northeast extremity of Beringia, and arctic ocean sedimentation. Quat. Sci. Rev. 28, 1573–1596. https://doi.org/10.1016/j.quascirev.2009.04.006.

French, H.M., Harry, D.G., 1990. Observations on buried glacier ice and massive segregated ice, western arctic coast, Canada. Permafr. Periglac. Process. 1, 31–43. https://doi.org/10.1002/ppp.3430010105.

French, H., Shur, Y., 2010. The principles of cryostratigraphy. Earth Sci. Rev. 101, 190–206. https://doi.org/10.1016/j.earscirev.2010.04.002.

Fritz, M., Wetterich, S., Meyer, H., Schirrmeister, L., Lantuit, H., Pollard, W.H., 2011. Origin and characteristics of massive ground ice on Herschel Island (western Canadian Arctic) as revealed by stable water isotope and hydrochemical signatures. Permafr. Periglac. Process. 22, 26–38. https://doi.org/10.1002/ppp.714.

Fritz, M., Wetterich, S., Schirrmeister, L., Meyer, H., Lantuit, H., Preusser, F., Pollard, W. H., 2012. Eastern Beringia and beyond: late wisconsinan and Holocene landscape dynamics along the Yukon Coastal Plain, Canada. Palaeogeogr. Palaeoclimatol. Palaeoecol. 319–320, 28–45. https://doi.org/10.1016/j.palaeo.2011.12.015.

Fritz, M., Opel, T., Tanski, G., Herzschuh, U., Meyer, H., Eulenburg, A., Lantuit, H., 2015. Dissolved organic carbon (DOC) in Arctic ground ice. Cryosphere 9, 737–752. https://doi.org/10.5194/tc-9-737-2015.

Fritz, M., Wolter, J., Rudaya, N., Palagushkina, O., Nazarova, L., Obu, J., Rethemeyer, J., Lantuit, H., Wetterich, S., 2016. Holocene ice-wedge polygon development in the northern Yukon, Canada. Quat. Sci. Rev. 147, 279–297. https://doi.org/10.1016/j.quascirev.2016.02.008.

Fritz, M., Unkel, I., Lenz, J., Gajewski, K., Frenzel, P., Paquette, N., Lantuit, H., Körte, L., Wetterich, S., 2018. Regional environmental change versus local signal preservation in Holocene thermokarst lake sediments: a case study from Herschel Island, Yukon (Canada). J. Paleolimnol. 60, 77–96. https://doi.org/10.1007/s10933-018-0025-0, 2018.

Fritz, M., Herzschuh, U., Wetterich, S., Lantuit, H., Fritz, M., Wetterich, S., McAlister, J., Meyer, H., 2022. A new local meteoric water line for Inuvik (NT, Canada). Earth Syst. Sci. Data 14, 57–63. https://doi.org/10.5194/essd-14-57-2022.

Grinter, M., Lacelle, D., Baranova, N., Murseli, S., Clark, I., 2019. Late Pleistocene and Holocene ice-wedge activity on the blackstone plateau, central Yukon, Canada. Quat. Res. 91 (1), 179–193. https://doi.org/10.1017/qua.2018.65.

Günther, F., Overduin, P.P., Sandakov, A.V., Grosse, G., Grigoriev, M.N., 2013. Short- and long-term thermo-erosion of ice-rich permafrost coasts in the Laptev Sea region. Biogeosciences 10, 4297–4318. https://doi.org/10.5194/bg-10-4297-2013.

Günther, F., Overduin, P.P., Yakshina, I.A., Opel, T., Baranskaya, A.V., Grigoriev, M.N., 2015. Observing Muostakh disappear: permafrost thaw subsidence and erosion of a ground-ice-rich island in response to arctic summer warming and sea ice reduction. Cryosphere 9, 151–178. https://doi.org/10.5194/tc-9-151-2015.

Guo, L., Macdonald, R.W., 2006. Source and transport of terrigenous organic matter in the upper Yukon River: evidence from isotope (δ13C, Δ14C, and δ15N) composition of dissolved, colloidal, and particulate phases. Global Biogeochem. Cycles 20, GB2011. https://doi.org/10.1029/2005GB002593.

Harington, C.R., 1989. Pleistocene vertebrate localities in the Yukon. In: Carter, L.D., Hamilton, T.D., Galloway, J.P. (Eds.), Late Cenozoic History of the Interior Basins of Alaska and the Yukon, vol. 1026. U.S. Geological Survey Circular, pp. 93–98.

Harington, C.R. (Ed.), 2003. Annotated Bibliography of Quaternary Vertebrates of Northern North America – with Radiocarbon Dates. University of Toronto Press, Toronto, p. 360.

Holland, K.M., Porter, T.J., Froese, D.G., Kokelj, S.V., Buchanan, C.A., 2020. Ice-wedge evidence of Holocene winter warming in the Canadian Arctic. Geophys. Res. Lett. 47, e2020GL087942 https://doi.org/10.1029/2020gl087942.

Ingólfsson, Ó., Lokrantz, H., 2003. Massive ground ice body of glacial origin at Yugorski Peninsula, arctic Russia. Permafr. Periglac. Process. 14, 199–215. https://doi.org/10.1002/ppp.455.

Kaufman, D.S., Ager, T.A., Anderson, N.J., Anderson, P.M., Andrews, J.T., Bartlein, P.J., Brubaker, L.B., Coats, L.L., Cwynar, L.C., Duvall, M.L., Dyke, A.S., Edwards, M.E.,

Eisner, W.R., Gajewski, K., Geirsdottir, A., Hu, F.S., Jennings, A.E., Kaplan, M.R., Kerwin, M.W., Lozhkinm, A.V., MacDonald, G.M., Miller, G.H., Mock, C.J., Oswald, W.W., Otto-Bliesner, B.L., Porinchu, D.F., Rühland, K., Smol, J.P., Steig, E. J., Wolfe, B.B., 2004. Holocene thermal maximum in the western Arctic (0–180°W). Quat. Sci. Rev. 23 (18–19), 529–560. https://doi.org/10.1016/j. quascirev.2003.09.007.

Kennedy, K.E., Froese, D.G., Zazula, G.D., Lauriol, B., 2010. Last Glacial Maximum age for the northwest Laurentide maximum from the Eagle River spillway and delta complex, northern Yukon. Quat. Sci. Rev. 29, 1288–1300. https://doi.org/10.1016/j.quascirev.2010.02.015.

Khomutov, A., Leibman, M., Dvornikov, Yu, Gubarkov, A., Mullanurov, D., Khairullinet, R., 2017. Activation of cryogenic earth flows and formation of thermocirques on Central Yamal as a result of climate fluctuation. In: Mikoš, M., Vilímek, V., Yin, Y., Sassa, K. (Eds.), Advancing Culture of Living with Landslides. World Landslide Forum 2017. Springer, Cham, Switzerland, pp. 209–216. https://doi.org/10.1007/978-3-319-53483-1_24.

Kizyakov, A.I., Leibman, M.O., Perednya, D.D., 2006. Destructive relief-forming processes at the coasts of the plains with tabular ground ice. Kriosfera Zemli (Earth Cryosphere) X (2), 79–89 (in Russian).

Kizyakov, A.I., Zimin, M.V., Leibman, M.O., Pravikova, N.V., 2013. Monitoring of the rate of thermal denudation and thermal abrasion on the western coast of Kolguev Island, using high resolution satellite images. Kriosfera Zemli (Earth Cryosphere) XVII, 36–47 (in Russian).

Kizyakov, A.I., Wetterich, S., Günther, F., Opel, T., Jongejans, L.L., Courtin, J., Meyer, H., Shepelev, A.G., Syromyatnikov, I.I., Fedorov, A.N., Zimin, M.V., Grosse, G., 2023. Landforms and degradation pattern of the Batagay thaw slump, Northeastern Siberia. Geomorphology 420, 108501. https://doi.org/10.1016/j.geomorph.2022.108501.

Kokelj, S.V., Lewkowicz, A.G., 1999. Salinization of permafrost terrain due to natural geomorphic disturbance, fosheim peninsula, Ellesmere island. Arctic 52 (4), 372–385. https://doi.org/10.14430/arctic942.

Kokelj, S.V., Lantz, T.C., Kanigan, J., Smith, S.L., Coutts, R., 2009. Origin and polycyclic behaviour of tundra thaw slumps, Mackenzie Delta region, Northwest Territories, Canada. Permafr. Periglac. Process. 20, 173–184. https://doi.org/10.1002/ppp.642.

Kokelj, S.V., Lantz, T.C., Tunnicliffe, J., Segal, R., Lacelle, D., 2017. Climate-driven thaw of permafrost preserved glacial landscapes, northwestern Canada. Geology 45 (4), 371–374. https://doi.org/10.1130/G38626.1.

Kunitsky, V.V., Syromyatnikov, I., Schirrmeister, L., Skachov, Y.B., Grosse, G., Wetterich, S., Grigoriev, M.N., 2013. Ice-rich permafrost and thermal denudation in the Batagay area (yana upland, east Siberia). Kriosfera Zemli (Earth Cryosphere) XVII (1), 56–58 (in Russian).

Lacelle, D., Vasil`chuk, Y.K., 2013. Recent progress (2007–2012) in permafrost isotope geochemistry. Permafr. Periglac. Process. 24, 138–145. https://doi.org/10.1002/ppp.1768.

Lacelle, D., Bjornson, J., Lauriol, B., Clark, I.D., Troutet, Y., 2004. Segregated-intrusive ice of subglacial meltwater origin in retrogressive thaw flow headwalls, Richardson Mountains, NWT, Canada. Quat. Sci. Rev. 23, 681–696. https://doi.org/10.1016/j.quascirev.2003.09.005.

Lacelle, D., Brooker, A., Fraser, R.H., Kokelj, S.V., 2015. Distribution and growth of thaw slumps in the Richardson Mountains–Peel Plateau region, northwestern Canada. Geomorphology 235, 40–51. https://doi.org/10.1016/j.geomorph.2015.01.024.

Lacelle, D., Fisher, D.A., Coulombe, S., Fortier, D., Frappier, R., 2018. Buried remnants of the Laurentide Ice Sheet and connections to its surface elevation. Sci. Rep. 8, 13286 https://doi.org/10.1038/s41598-018-31166-2.

Lachenbruch, A.H., 1962. Mechanics of thermal contraction cracks and ice-wedge polygons in permafrost. GSA (Geol. Soc. Am.) Spec. Pap. (Reg. Stud.) 70, 1–66. https://doi.org/10.1130/SPE70-p1.

Lachniet, M.S., Lawson, D.E., Sloat, A.R., 2012. Revised C-14 dating of ice wedge growth in interior Alaska (USA) to MIS 2 reveals cold paleoclimate and carbon recycling in ancient permafrost terrain. Quat. Res. 78, 217–225. https://doi.org/10.1016/j.yqres.2012.05.007.

Lakeman, T.R., England, J.H., 2012. Paleoglaciological insights from the age and morphology of the Jesse moraine belt, western Canadian Arctic. Quat. Sci. Rev. 47, 82–100. https://doi.org/10.1016/j.quascirev.2012.04.018.

Lantuit, H., Pollard, W.H., 2008. Fifty years of coastal erosion and retrogressive thaw slump activity on Herschel Island, southern Beaufort Sea, Yukon Territory, Canada. Geomorphology 95, 84–102. https://doi.org/10.1016/j.geomorph.2006.07.040.

Lantuit, H., Pollard, W.H., Couture, N., Fritz, M., Schirrmeister, L., Meyer, H., Hubberten, H.-W., 2012. Modern and late Holocene retrogressive thaw slump activity on the Yukon Coastal Plain and Herschel island, Yukon territory, Canada. Permafr. Periglac. Process. 23, 39–51. https://doi.org/10.1002/ppp.1731.

Lantz, T.C., Kokelj, S.V., 2008. Increasing rates of retrogressive thaw slump activity in the Mackenzie Delta region. Geophys. Res. Lett. 35, L06502 https://doi.org/10.1029/2007GL032433. N.W.T., Canada.

Leibman, M., Kizyakov, A., Zhdanova, Y., Sonyushkin, A., Zimin, M., 2021. Coastal retreat due to thermodenudation on the Yugorsky Peninsula, Russia during the last decade, update since 2001–2010. Rem. Sens. 13 (20) https://doi.org/10.3390/rs13204042, 4042–4042.

Lenz, J., Fritz, M., Schirrmeister, L., Lantuit, H., Wooller, M.J., Pollard, W.H., Wetterich, S., 2013. Periglacial landscape dynamics in the western Canadian Arctic: results from a thermokarst lake record on a push moraine (Herschel Island, Yukon Territory). Palaeogeogr. Palaeoclimatol. Palaeoecol. 381–382, 15–25. https://doi.org/10.1016/j.palaeo.2013.04.009.

Lewkowicz, A.G., Way, R.G., 2019. Extremes of summer climate trigger thousands of thermokarst landslides in a High Arctic environment. Nat. Commun. 10, 1329. https://doi.org/10.1038/s41467-019-09314-7.

Lorrain, R.D., Demeur, P., 1985. Isotopic evidence for relic Pleistocene glacier ice on Victoria island, Canadian arctic Archipelago. Arct. Alp. Res. 17, 89–98. https://doi.org/10.2307/1550964.

Mackay, J.R., 1959. Glacier ice-thrust features of the Yukon coast. Geogr. Bull. 13, 5–21.

Mackay, J.R., Dallimore, S.R., 1992. Massive ice of the Tuktoyaktuk area, western Arctic coast, Canada. Can. J. Earth Sci. 29, 1235–1249. https://doi.org/10.1139/e92-099.

Maslakov, A., Zotova, L., Komova, N., Grishchenko, M., Zamolodchikov, D., Zelensky, G., 2021. Vulnerability of the permafrost landscapes in the eastern Chukotka coastal plains to human impact and climate change. Land 10 (5), 445. https://doi.org/10.3390/land10050445.

Meyer, H., Schönicke, L., Wand, U., Hubberten, H.-W., Friedrichsen, H., 2000. Isotope studies of hydrogen and oxygen in ground ice – experiences with the equilibration technique. Isot. Environ. Health Stud. 36, 133–149. https://doi.org/10.1080/10256010008032939.

Meyer, H., Schirrmeister, L., Yoshikawa, K., Opel, T., Wetterich, S., Hubberten, H.-W., Brown, J., 2010. Permafrost evidence for severe winter cooling during the Younger Dryas in northern Alaska. Geophys. Res. Lett. 37, L03501 https://doi.org/10.1029/2009gl041013.

Meyer, H., Opel, T., Laepple, T., Dereviagin, A.Y., Hoffmann, K., Werner, M., 2015. Long-term winter warming trend in the Siberian Arctic during the mid- to late Holocene. Nat. Geosci. 8, 122–125. https://doi.org/10.1038/ngeo2349.

Michel, F.A., 1990. Isotopic composition of ice-wedge ice in northwestern Canada. Proceedings of the Fifth Canadian Permafrost Conference. Collect. Nord. 54, 5–9.

Mollenhauer, G., Grotheer, H., Gentz, T., Bonk, E., Hefter, J., 2021. Standard operation procedures and performance of the MICADAS radiocarbon laboratory at Alfred Wegener Institute (AWI), Germany. Nucl. Instrum. Methods Phys. Res. B: Beam Interact. Mater. At. 496, 45–51. https://doi.org/10.1016/j.nimb.2021.03.016.

Moorman, B.J., Michel, F.A. and Wilson, A., 1996. ^{14}C dating of trapped gases in massive ground ice, Western Canadian Arctic. Permafr. Periglac. Process. 7, 257-266. doi: 10.1002/(SICI)1099-1530(199609)7:3<257::AID-PPP220>3.0.CO;2-P.

Murton, J.B., French, H.M., Lamothe, M., 1997. Late Wisconsinan erosion and eolian deposition, Summer Island area, Pleistocene Mackenzie Delta, Northwest Territories: optical dating and implications for glacial chronology. Can. J. Earth Sci. 34, 190–199. https://doi.org/10.1139/e17-015.

Murton, J.B., Whiteman, C.A., Waller, R.I., Pollard, W.H., Clark, I.D., Dallimore, S.R., 2005. Basal ice facies and supraglacial melt-out till of the Laurentide ice sheet, Tuktoyaktuk coastlands, western arctic Canada. Quat. Sci. Rev. 24, 681–708. https://doi.org/10.1016/j.quascirev.2004.06.008.

Murton, J.B., Frechen, M., Maddy, D., 2007. Luminescence dating of mid- to late wisconsinan aeolian sand as a constraint on the last advance of the Laurentide ice sheet across the Tuktoyaktuk coastlands, western arctic Canada. Can. J. Earth Sci. 44, 857–869. https://doi.org/10.1139/e07-015.

Murton, J.B., Opel, T., Toms, P., Blinov, A., Fuchs, M., Wood, J., Gärtner, A., Merchel, S., Rugel, G., Savvinov, G., Wetterich, S., 2022. A multimethod dating study of ancient permafrost, Batagay megaslump, east Siberia. Quat. Res. 105, 1–22. https://doi.org/10.1017/qua.2021.27.

Nesterova, N.B., Khomutov, A.V., Leibman, M.O., Safonov, T.A., Belova, N.G., 2021. The inventory of retrogressive thaw slumps (thermocirques) in the North of West Siberia based on 2016-2018 satellite imagery mosaic. Kriosfera Zemli (Earth Cryosphere) XXV (6), 41–50. https://doi.org/10.15372/KZ20210604 (in Russian).

Obu, J., Lantuit, H., Fritz, M., Pollard, W.H., Sachs, T., Günther, F., 2016. Relation between planimetric and volumetric measurements of permafrost coast erosion: a case study from Herschel Island, western Canadian Arctic. Polar Res. 35, 3031. https://doi.org/10.3402/polar.v35.30313.

Obu, J., Lantuit, H., Grosse, G., Günther, F., Sachs, T., Helm, V., Fritz, F., 2017. Coastal erosion and mass wasting along the Canadian Beaufort Sea based on annual airborne LiDAR elevation data. Geomorphology 293, 331–346. https://doi.org/10.1016/j.geomorph.2016.02.014.

Obu, J., Westermann, S., Bartsch, A., Berdnikov, N., Christiansen, H.H., Dashtseren, A., et al., 2019. Northern Hemisphere permafrost map based on TTOP modeling for 2000–2016 at 1 km^2 scale. Earth Sci. Rev. 193, 299–316. https://doi.org/10.1016/j.earscirev.2019.04.023.

Opel, T., Laepple, T., Meyer, H., Dereviagin, A.Y., Wetterich, S., 2017. Northeast Siberian ice wedges confirm Arctic winter warming over the past two millennia. Holocene 27, 1789–1796. https://doi.org/10.1177/0959683617702229.

Opel, T., Meyer, H., Wetterich, S., Laepple, T., Dereviagin, A., Murton, J., 2018. Ice wedges as archives of winter paleoclimate: a review. Permafr. Periglac. Process. 29, 199–209. https://doi.org/10.1002/ppp.1980.

Opel, T., Murton, J.B., Wetterich, S., Meyer, H., Ashastina, K., Günther, F., Grotheer, H., Mollenhauer, G., Danilov, P.P., Boeskorov, V., Savvinov, G.N., Schirrmeister, L., 2019. Past climate and continentality inferred from ice wedges at Batagay megaslump in the Northern Hemisphere's most continental region, Yana Highlands, interior Yakutia. Clim. Past 15, 1443–1461. https://doi.org/10.5194/cp-15-1443-2019.

Parmuzin, S.Y., Sukhodol`skiy, S.E., 1982. Massive ice of the Central Yamal and its role in the relief formation. In: Popov, A.I. (Ed.), Massive Ice in Cryolithozone. Melnikov Permafrost Institute, Yakutsk, pp. 51–61 (in Russian).

Pautler, B.G., Woods, G.C., Dubnick, A., Simpson, A.J., Sharp, M.J., Fitzsimons, S.J., Simpson, M.J., 2012. Molecular Characterization of dissolved organic matter in glacial ice: coupling natural abundance 1H NMR and fluorescence spectroscopy. Environ. Sci. Technol. 46 (7), 3753–3761. https://doi.org/10.1021/es203942y.

Pizhankova, E.I., Dobrynina, M.S., 2010. The dynamics of the Lyakhovsky Island coastline (Results of aerospace image interpretation). Kriosfera Zemli (Earth Cryosphere) XIV (4), 66–79 (in Russian).

Pollard, W.H., 1990. The nature and origin of ground ice in the Herschel Island area, Yukon Territory. In: Proceedings of the Fifth Canadian Permafrost Conference, vol. 54, pp. 23–30. Collection Nordicana.

Porter, T.J., Opel, T., 2020. Recent advances in paleoclimatological studies of Arctic wedge- and pore-ice stable-water isotope records. Permafr. Periglac. Process. 31, 429–441. https://doi.org/10.1002/ppp.2052.

Ramage, J.L., Irrgang, A.M., Herzschuh, U., Morgenstern, A., Couture, N., Lantuit, H., 2017. Terrain controls on the occurrence of coastal retrogressive thaw slumps along the Yukon Coast, Canada. J. Geophys. Res. Earth Surf. 122, 1619–1634. https://doi.org/10.1002/2017JF004231.

Rampton, V.N., 1982. Quaternary geology of the Yukon Coastal Plain. Geol. Surv. Can. Bull. 317, 49. https://doi.org/10.4095/111347.

Rampton, V.N., 1988. Quaternary Geology of the Tuktoyaktuk Coastlands, Northwest Territories, vol. 423. Geological Survey of Canada, Memoir, p. 98.

Rampton, V.N., 1991. Observations on buried glacier ice and massive segregated ice, Western Arctic Coast, Canada: discussion. Permafr. Periglac. Process. 2, 163–165. https://doi.org/10.1002/ppp.3430020209.

Rampton, V.N., Mackay, J.R., 1971. Massive Ice and Icy Sediments throughout the Tuktoyaktuk Peninsula, Richards Island and Nearby Areas, District of Mackenzie. Geological Survey of Canada, p. 16. Paper 71- 21.

Reimer, P., Austin, W.E.N., Bard, E., Bayliss, A., Blackwell, P.G., Bronk Ramsey, C., Butzin, M., Edwards, R.L., Friedrich, M., Grootes, P.M., Guilderson, T.P., Hajdas, I., Heaton, T.J., Hogg, A., Kromer, B., Manning, S.W., Muscheler, R., Palmer, J.G., Pearson, C., van der Plicht, J., Reim Richards, D.A., Scott, E.M., Southon, J.R., Turney, C.S.M., Wacker, L., Adolphi, F., Büntgen, U., Fahrni, S., Fogtmann-Schulz, A., Friedrich, R., Köhler, P., Kudsk, S., Miyake, F., Olsen, J., Sakamoto, M., Sookdeo, A., Talamo, S., 2020. The IntCal20 Northern Hemisphere radiocarbon age calibration curve (0-55 cal k BP). Radiocarbon 62, 725–757. https://doi.org/10.1017/RDC.2020.41.

Ritchie, J.C., 1984. Past and Present Vegetation of the Far Northwest of Canada. University of Toronto Press, Toronto, p. 251.

Runge, A., Nitze, I., Grosse, G., 2022. Remote sensing annual dynamics of rapid permafrost thaw disturbances with LandTrendr. Rem. Sens. Environ. 268, 112752 https://doi.org/10.1016/j.rse.2021.112752.

Schirrmeister, L., Froese, D., Tumskoy, V., Grosse, G., Wetterich, S., 2013. Permafrost and Periglacial Features | Yedoma: Late Pleistocene ice-rich syngenetic permafrost of Beringia. In: Elias, S.A., Mock, C.J. (Eds.), *Encyclopedia of Quaternary Sciences*, Second edition. Elsevier, Amsterdam, The Netherlands, pp. 542–552. https://doi.org/10.1016/b978-0-444-53643-3.00106-0.

Segal, R.A., Lantz, T.C., Kokelj, S.V., 2016. Acceleration of thaw slump activity in glaciated landscapes of the Western Canadian Arctic. Environ. Res. Lett. 11 (3), 034025 https://doi.org/10.1088/1748-9326/11/3/034025.

Streletskaya, I.D., Ukraintseva, N.G., Drozdov, I.D., 2002. In: Late Pleistocene History Reconstruction Based on the Massive Ground Ice Origin in the Arctic Coastal Zone (Massive Ground Ice Database). Moscow State University, Institute of Geography, Department of Cryolithology and Glaciology, Moscow, Russia. Database, last access: 22–10–04. http://www.geogr.msu.ru/cafedra/crio/nauchd/napr/ice/.

Streletskaya, I.D., Vasiliev, A.A., Oblogov, G.E., Matyukhin, A.G., 2013. Isotopic composition on ground ice in western yamal (Marre-Sale). Ice and Snow (Led i Sneg) 53 (2), 83–92. https://doi.org/10.15356/2076-6734-2013-2-83-92 (in Russian).

Sun, S., Meyer, V.D., Dolman, A.M., Winterfeld, M., Hefter, J., Dummann, W., McIntyre, C., Montluçon, D., Haghipour, N., Wacker, L., Gentz, T., van der Voort, T., Eglinton, T.I., Mollenhauer, G., 2020. [14]C blank assessment in small-scale compound-specific radiocarbon analysis of lipid biomarkers and lignin phenols. Radiocarbon 62 (1), 207–218. https://doi.org/10.1017/RDC.2019.108.

Tanski, G., Couture, N., Lantuit, H., Eulenburg, A., Fritz, M., 2016. Eroding permafrost coasts release low amounts of dissolved organic carbon (DOC) from ground ice into the nearshore zone of the Arctic Ocean. Global Biogeochem. Cycles 30, 1054–1068. https://doi.org/10.1002/2015GB005337.

Wacker, L., Němec, M., Bourquin, J., 2010. A revolutionary graphitisation system: fully automated, compact and simple. Nucl. Instrum. Methods Phys. Res. B: Beam Interact. Mater. At. 268, 931–934. https://doi.org/10.1016/j.nimb.2009.10.067.

Walker, D.A., Raynolds, M.K., Daniëls, F.J., Einarsson, E., Elvebakk, A., Gould, W.A., Katenin, A.E., Kholod, S.S., Markon, C.J., Melnikov, E.S., Moskalenko, N.G., Talbot, S.S., Yurtsev, B.A., the other members of the CAVM Team, 2005. The circumpolar Arctic vegetation map. J. Veg. Sci. 16, 267–282. https://doi.org/10.1111/j.1654-1103.2005.tb02365.x.

Wang, B., Paudel, B., Li, H., 2016. Behaviour of retrogressive thaw slumps in northern Canada — three-year monitoring results from 18 sites. Landslides 13, 1–8. https://doi.org/10.1007/s10346-014-0549-y.

Ward Jones, M.K., Pollard, W.H., Jones, B.M., 2019. Rapid initialization of retrogressive thaw slumps in the Canadian high Arctic and their response to climate and terrain factors. Environ. Res. Lett. 14, 055006 https://doi.org/10.1088/1748-9326/ab12fd.

Wetterich, S., Kizyakov, A., Fritz, M., Wolter, J., Mollenhauer, G., Meyer, H., Fuchs, M., Aksenov, A., Matthes, H., Schirrmeister, L., Opel, T., 2020. The cryostratigraphy of the Yedoma Cliff of Sobo-Sise Island (Lena delta) reveals permafrost dynamics in the central Laptev Sea coastal region during the last 52 kyr. Cryosphere 14, 4525–4551. https://doi.org/10.5194/tc-14-4525-2020.

Wetterich, S., Meyer, H., Fritz, M., Mollenhauer, G., Rethemeyer, J., Kizyakov, A., Schirrmeister, L., Opel, T., 2021. Northeast Siberian permafrost ice-wedge stable isotopes depict pronounced Last Glacial Maximum winter cooling. Geophys. Res. Lett. 48, e2020GL092087 https://doi.org/10.1029/2020GL092087.

Wolter, J., Lantuit, H., Fritz, M., Macias-Fauria, M., Myers-Smith, I., Herzschuh, U., 2016. Vegetation composition and shrub extent on the Yukon coast, Canada, are strongly linked to ice-wedge polygon degradation. Polar Res. 35 (1), 27489 https://doi.org/10.3402/polar.v35.27489.

Zazula, G.D., Gregory Hare, P., Storer, J.E., 2009. New radiocarbon-dated vertebrate fossils from Herschel Island: implications for the palaeoenvironments and glacial chronology of the Beaufort Sea coastlands. Arctic 62 (3), 273–280. https://doi.org/10.14430/arctic147.